Optimal skyrmion stability in antisymmetric ultrathin ferromagnetic bilayers

Anne Bernand-Mantel,[1, *] Valeriy V. Slastikov,[2] and Cyrill B. Muratov[3]
[1] *Université de Toulouse, CNRS, CEMES, Toulouse, France*
[2] *School of Mathematics, University of Bristol, Bristol BS8 1UG, United Kingdom*
[3] *Dipartimento di Matematica, Università di Pisa, Largo B. Pontecorvo, 5, 56127 Pisa, Italy*

(Dated: April 2, 2026)

We demonstrate the stray-field-mediated skyrmion stabilizing capabilities of ultrathin exchange-decoupled antisymmetric ferromagnetic bilayers based on conventional transition metal materials. Using an asymptotically exact micromagnetic model valid in the ultrathin film limit, we show that the antisymmetric tailoring of the bilayer allows the Dzyaloshinskii-Moriya interaction and the dipolar interaction to act synergistically to stabilize skyrmions, in contrast to the monolayer case, in which these energies compete. To obtain optimal stability of these skyrmions against collapse and bursting – the two fundamental processes determining skyrmion lifetime, we carry out an asymptotic analysis of the saddle point solution that separates the skyrmion from the demagnetized state. The result is an optimal stability line for compact skyrmions in the non-dimensional parameter space of the effective Dzyaloshinskii-Moriya interaction strength and the effective film thickness. Our predictions are confirmed by extensive micromagnetic simulations of antisymmetric bilayers, using magnetic parameters of the conventional Pt/Co/AlO$_x$ systems. Our results provide a new pathway for experimental observations of 10 nm radius zero-field skyrmions with lifetimes compatible with information technology applications.

I. INTRODUCTION

Magnetic skyrmions are topological solitons that are considered to be promising candidates for ultra-dense and energy-efficient information technology and unconventional computing applications [1–5]. The past decade has seen major theoretical and experimental efforts from the research community in material optimization towards observation of smaller and more stable magnetic skyrmions. Despite these efforts, a reproducible experimental realization of 10 nm isolated skyrmions at zero applied magnetic field with lifetimes exceeding several seconds at room temperature remains elusive.

In single ultrathin ferromagnetic layers with broken inversion symmetry, compact skyrmions with diameters down to 1 nm have been reported under magnetic fields of a few Tesla in PdFe/Ir(111) at liquid helium temperature [6]. More recently, a 5 nm diameter skyrmion was observed at 4.2K in Rh/Co/Ir(111) at zero applied magnetic field [7]. A way to enhance the skyrmion lifetime in order to make them observable at room temperature (RT) is to stack several asymmetrically capped ferromagnetic layers, as observed in the Ir/Co/Pt system where skyrmions with diameters down to 30 nm were recorded at RT [8]. In these multilayer systems, the stray field plays a non-negligible role in the stabilization of the observed skyrmionic bubbles [9]. This prevents the reduction of the size below a certain value due to the existence of an energy saddle that separates the compact skyrmion, usually unstable at RT, from the experimentally observed skyrmionic bubble [10, 11]. The current-driven dynamics of these skyrmionic bubbles was also found to be hindered by disorder [12, 13], as well as by the non-uniformity of the magnetization in the direction perpendicular to the sample plane [9].

Another general issue related to the dynamics of skyrmions is their tendency to move non-collinearly with the applied electric current [14], a phenomenon referred to as skyrmion Hall effect that was predicted in the early works on skyrmions [15]. A promising direction to reduce the skyrmion Hall effect is to use rare-earth transition metal ferrimagnets, in which the gyroscopic force generated by each magnetic sublattice is canceled at the compensation temperature [16, 17]. Although high current-induced skyrmion velocities have been reported in such films [17–19], this system seems to generally suffer from the same limitation as ferromagnetic thin films, namely, the difficulty to stabilize compact skyrmions at room temperature and zero applied magnetic field, and there exists only a single report of sub 20 nm diameter compact skyrmions [18] that has not been later reproduced.

The attention has recently shifted towards another system: the synthetic antiferromagnet (SAF) system made of two ferromagnetic layers with broken inversion symmetry, coupled antiferromagnetically via a metallic non-magnetic spacer. This system offers the same advantages as the compensated ferrimagnets in terms of high current-induced skyrmion velocity and vanishing skyrmion Hall effect [20–24], as well as a possibility to reach the flow regime for skyrmion current-induced motion, as was recently demonstrated [21, 22, 24]. On the other hand, issues have emerged in this system such as the coexistence of ferromagnetic and antiferromagnetic phases [25–27] and the existence of skyrmion inertia and a maximum velocity limit related to the finite interlayer antiferromagnetic coupling [28]. In addition,

---

* anne.bernand-mantel@cemes.fr

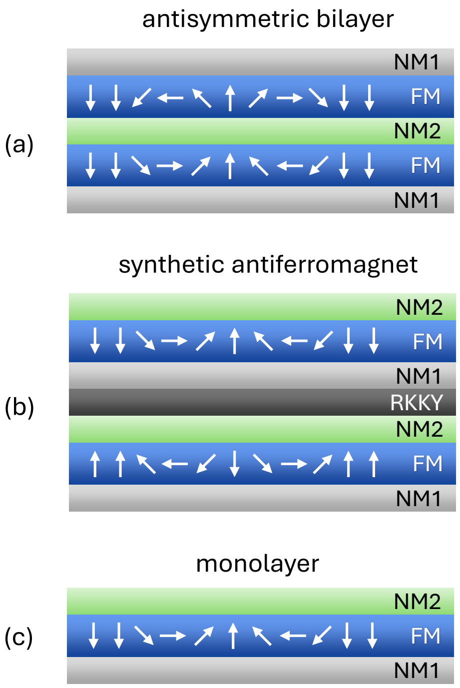

FIG. 1. Schematics of the ferromagnetic multilayer structures with a skyrmion present: (a) antisymmetric ferromagnetic bilayer consisting of two identical ferromagnetic layers separated by a single non-magnetic layer (NM2) and capped by a different non-magnetic material (NM1); (b) a SAF consisting of two ferromagnetic layers (FM) capped by two different non-magnetic layers (NM1 and NM2) and separated by an exchange coupler (RKKY); (c) single ferromagnetic monolayer (FM) capped by two different non-magnetic layers (NM1 and NM2).

the property of SAF having a vanishing stray field due to the antiparallel alignment of the magnetization vector in the two layers makes the experimental observation of skyrmions even more challenging than in the case of single ferromagnets and ferromagnetically coupled multilayers. In a fully compensated SAF with no stray field, skyrmionic bubbles are ruled out and only zero-field compact skyrmions should be observed. In theory, stacking several layers of compensated SAF could lead to an increase of the collapse barrier of individual compact skyrmions [22, 29], while not increasing their size. However, the experimentally observed skyrmions remain in a few hundred nanometer to a few micron diameter range and suffer from stripe-out instabilities [20–23]. This reveals their skyrmionic bubble nature caused by the presence of residual stray fields [29, 30] due to the finite thickness of the layers and the finite distance separating them. This issue has not been resolved, despite significant efforts in material optimization [29, 31].

The effect of stray field on domain walls and skyrmionic bubbles in multilayers is a well studied phenomenon that gives rise to a magnetization twist in the out-of-plane direction in multilayers [9, 32–36] and antiparallel domain wall configurations in bilayers [37, 38]. In a recent study, we demonstrated that in ultrathin multilayers the interlayer dipolar interaction is taking the form of a DMI-like energy term which contributes to this twist [39] (see also [36, 40]). Our result was applied to the case of stray field-coupled ferromagnetic bilayers in the absence of DMI, for which we obtained minimizers in the form of a pair of Néel skyrmions with opposite chiralities fixed by the flux-closure pattern. Exploiting this stray-field-minimizing configuration to stabilize skyrmions in antisymmetric ferromagnetic bilayers with opposite DMI remains largely unexplored. To date, there have been only two experimental studies reporting on skyrmionic bubbles in this system [40, 41]. In the most recent work [40], the contribution from the DMI-like energy term of dipolar origin to the wall energy has been estimated with the help of relevant analytical models [36] and micromagnetic simulations.

In the present work, we explore the potential of antisymmetric ferromagnetic bilayers for the realization of compact and stable skyrmions compatible with memory applications. To this aim, we derive a reduced thin-film micromagnetic energy functional describing the magnetization configurations in stacked ultrathin ferromagnetic layers and identify just two dimensionless parameters – the reduced DMI strength and the reduced film thickness, governing the system's behavior. We next focus on the antisymmetric ferromagnetic bilayer system, for which we demonstrate existence of skyrmionic states (pairs of Néel skyrmions, one per layer) as local energy minimizers and identify the approximate boundary of the parameter region beyond which these skyrmion states undergo bursting and strip-out. We then locate an approximate optimal stability curve in the two-dimensional parameter space, over which the bursting energy barrier is equal to the collapse barrier, signifying the parameters at which the skyrmion is most stable with respect to thermal noise.

Starting with this curve, we then carry out a two-dimensional parameter sweep to numerically obtain a detailed phase diagram of skyrmion solutions existence, along with their radii and the energy barriers as functions of the reduced DMI strength and the reduced film thickness. We repeat this process for ferromagnetic monolayers and then carry out a comparison between antisymmetric ferromagnetic bilayers, SAF and ferromagnetic monolayers. Our results show that, for typical magnetic parameters of transition metal multilayers, antisymmetric bilayers exhibit a wide range of conditions under which room-temperature-stable magnetic skyrmions with radii on the order of 10 nm can exist. This is due to the synergistic action of the interfacial DMI and the dipolar interactions in antisymmetric exchange-decoupled ferromagnetic bilayers. The stability properties of these skyrmions compare favorably with those of the skyrmions in SAF and monolayers.

The paper is organized as follows. In Sec. II, we present the basic micromagnetic model and then carry out its thin fim reduction, followed by non-dimensionalization. In Sec. III, we present a detailed analysis of the reduced thin film micromagnetic energy for antisymmetric bilayers. In Sec. IV, we carry out an analogous study for SAF and single ferromagnetic monolayers and compare the results with those for antisymmetric bilayers. Finally, in Sec. V we draw conclusions.

II. MODEL

Our starting point is the micromagnetic energy of a stack of identical ferromagnetic layers in the presence of intralayer exchange, perpendicular magnetocrystalline anisotropy (both of bulk and interfacial origin), interfacial DMI and the magnetostatic interaction [39, 42, 43]. Consider N stacked layers of a single ferromagnetic material of thickness d separated by non-magnetic layers of thickness $(a-1)d$, where $a > 1$ is a geometric factor corresponding to the ratio of the total thickness of the stack unit to that of the ferromagnet. The ferromagnet is characterized by saturation magnetization M_s (in A/m) and exchange stiffness A (in J/m). For $n = 1, \ldots, N$, the n-th ferromagnetic layer is assumed to occupy the region of space

$$\begin{aligned}\Omega_n = \big\{ & (x,y,z) \in \mathbb{R}^3 \ : \\ & (x,y) \in \mathbb{R}^2, \ z \in [ad(n-1), ad(n-1)+d] \big\}. \qquad (1)\end{aligned}$$

Each layer Ω_n has bulk uniaxial perpendicular magnetocrystalline anisotropy constant K_u (in J/m^3), interfacial anisotropy constants $K_n^{s,\pm}$ (in J/m^2) on the top and bottom surfaces $\partial\Omega_n^\pm$ of Ω_n, and interfacial DMI strengths $D_n^{s,\pm}$ (in J/m) on $\partial\Omega_n^\pm$, respectively.

The energy of such a system takes the following form, in the SI units [39]:

$$\begin{aligned}\mathcal{E}(\mathbf{M}) = & \sum_{n=1}^N \int_{\Omega_n} \left\{ \frac{A}{M_s^2} |\nabla \mathbf{M}|^2 + \frac{K_u}{M_s^2} |\mathbf{M}^\perp|^2 \right\} d^3 r \\ & - \frac{\mu_0}{2} \sum_{n=1}^N \int_{\Omega_n} \left(\mathbf{H}_d \cdot \mathbf{M} + M_s^2 \right) d^3 r \\ & + \sum_{n=1}^N \left(\frac{K_n^{s,-}}{M_s^2} \int_{\partial\Omega_-} |\mathbf{M}^\perp|^2 d^2 r + \frac{K_n^{s,+}}{M_s^2} \int_{\partial\Omega_+} |\mathbf{M}^\perp|^2 d^2 r \right) \\ & - \sum_{n=1}^N \frac{D_n^{s,-}}{M_s^2} \int_{\partial\Omega_n^-} \left(M^\parallel \nabla \cdot \mathbf{M}^\perp - \mathbf{M}^\perp \cdot \nabla M^\parallel \right) d^2 r \\ & + \sum_{n=1}^N \frac{D_n^{s,+}}{M_s^2} \int_{\partial\Omega_n^+} \left(M^\parallel \nabla \cdot \mathbf{M}^\perp - \mathbf{M}^\perp \cdot \nabla M^\parallel \right) d^2 r. \qquad (2)\end{aligned}$$

Here $\mathbf{M} = (\mathbf{M}^\perp, M^\parallel)$ is the magnetization vector, whose in-plane component is $\mathbf{M}^\perp \in \mathbb{R}^2$ and the out-of-plane component is $M^\parallel \in \mathbb{R}$ (the superscripts are with respect to the direction of the easy axis $\hat{\mathbf{z}}$), with the convention that $|\mathbf{M}| = M_s$ in $\Omega = \bigcup_{n=1}^N \Omega_n$ and $|\mathbf{M}| = 0$ outside Ω. The first line in the energy represents the intralayer exchange plus the bulk perpendicular magnetocrystalline anisotropy, the second line gives the contribution of the magnetostatic energy of the demagnetizing field $\mathbf{H}_d$ vanishing for $z \to \pm\infty$ that solves the stationary Maxwell's equations

$$\nabla \cdot (\mathbf{H}_d + \mathbf{M}) = 0, \qquad \nabla \times \mathbf{H}_d = 0, \qquad (3)$$

from which we subtracted the contribution of the ferromagnetic state to avoid divergent integrals; the third line gives the magnetocrystalline anisotropy contributions of the bottom and top surfaces of each layer, and the last two lines give the respective DMI contributions of those surfaces. In writing the latter, we used the sign convention that yields the same DMI constants, $D_n^{s,+} = D_n^{s,-}$ for the interfaces between the ferromagnet with the same non-magnetic material on both sides of the ferromagnet. Notice that $\mathcal{E}(\mathbf{M}) = 0$ if $\mathbf{M} = \pm M_s \hat{\mathbf{z}}$ in Ω. Also notice that the gradient in the DMI contributions acts only in-plane, as the integrations there are carried out over the planes parallel to the xy-plane. Finally, for simplicity of the presentation we omitted the Zeeman energy term that can be easily added back to (2), if needed [44]. Other generalizations of the model, such as addition of the interlayer exchange coupling [45], or variable layer thicknesses and material parameters, are also straightforward.

We next carry out a non-dimensionalization of the energy in (2) by measuring lengths in the units of the exchange length $\ell_{ex} = \sqrt{A/K_d}$, where $K_d = \frac{1}{2}\mu_0 M_s^2$, introducing the normalized magnetization vector $\mathbf{m}(\mathbf{r}) = \mathbf{M}(\ell_{ex}\mathbf{r})/M_s$ for $\mathbf{r} \in \mathbb{R}^3$, and defining the dimensionless energy in the units of Ad, i.e., $E(\mathbf{m}) = \mathcal{E}(\mathbf{M})/(Ad)$. Then

$$\begin{aligned}E(\mathbf{m}) = & \frac{1}{\delta} \sum_{n=1}^N \int_{\ell_{ex}^{-1}\Omega_n} \left\{ |\nabla \mathbf{m}|^2 + Q_u |\mathbf{m}^\perp|^2 \right\} d^3 r \\ & - \frac{1}{\delta} \sum_{n=1}^N \int_{\ell_{ex}^{-1}\Omega_n} \left(\mathbf{h}_d \cdot \mathbf{m} + 1 \right) d^3 r \\ & + \sum_{n=1}^N Q_n^{s,-} \int_{\ell_{ex}^{-1}\partial\Omega_-} |\mathbf{m}^\perp|^2 d^2 r \\ & + \sum_{n=1}^N Q_n^{s,+} \int_{\ell_{ex}^{-1}\partial\Omega_+} |\mathbf{m}^\perp|^2 d^2 r \\ & - \sum_{n=1}^N \kappa_n^- \int_{\ell_{ex}^{-1}\partial\Omega_n^-} \left(m^\parallel \nabla \cdot \mathbf{m}^\perp - \mathbf{m}^\perp \cdot \nabla m^\parallel \right) d^2 r \\ & + \sum_{n=1}^N \kappa_n^+ \int_{\ell_{ex}^{-1}\partial\Omega_n^+} \left(m^\parallel \nabla \cdot \mathbf{m}^\perp - \mathbf{m}^\perp \cdot \nabla m^\parallel \right) d^2 r, \qquad (4)\end{aligned}$$

where, as before, $\mathbf{m} = (\mathbf{m}^\perp, m^\parallel)$, with $\mathbf{m}^\perp \in \mathbb{R}^2$ and $m^\parallel \in \mathbb{R}$ being the in-plane and out-of-plane components of $\mathbf{m}$, and we introduced the dimensionless film thickness $\delta = d/\ell_{ex}$ and the dimensionless quantities

$$Q_u = \frac{K_u}{K_d}, \quad Q_n^{s,\pm} = \frac{K_n^{s,\pm}}{dK_d}, \quad \kappa_n^{\pm} = \frac{D_n^{s,\pm}}{d\sqrt{AK_d}}, \qquad (5)$$

corresponding to the bulk anisotropy strength, surface anisotropy strengths and the DMI strengths, respectively. The rescaled demagnetizing field $\mathbf{h}_d$ satisfies

$$\mathbf{h}_d = -\nabla U, \qquad \Delta U = \nabla \cdot \mathbf{m}, \qquad (6)$$

in the sense of distributions in $\mathbb{R}^3$, with $\nabla U - \mathbf{m}$ vanishing at infinity [46].

The above model presents a formidable challenge to analysis and may in general only be treated through large-scale three-dimensional numerical simulations, using a number of available software packages (see, e.g., [47–52]). Nevertheless, this model may be considerably simplified in the case of ultrathin ferromagnetic layers that are relevant for most spintronic applications, where each material layer extends to thicknesses of only a few interatomic distances. It corresponds to an assumption that the total multilayer thickness is smaller than the exchange length in the material, $Nad \lesssim \ell_{ex}$. In this case the micromagnetic energy may be expanded in the powers of δ, keeping only the leading order terms (for a detailed derivation, see [39]). The micromagnetic energy then obeys $E(\mathbf{m}) \simeq E_N(\mathbf{m}_1, \ldots, \mathbf{m}_N)$, where $\mathbf{m}_n : \mathbb{R}^2 \to \mathbb{S}^2$ are the normalized magnetization vector fields in the n-th ferromagnetic layer that depend only on two spatial coordinates, and the reduced thin film energy E_N reads

$$\begin{aligned} E_N(\mathbf{m}_1, \ldots, \mathbf{m}_N) = \\ \sum_{n=1}^{N} \int_{\mathbb{R}^2} \left\{ |\nabla \mathbf{m}_n|^2 + (Q_n - 1)|\mathbf{m}_n^{\perp}|^2 \right\} d^2r \\ - \sum_{n=1}^{N} \int_{\mathbb{R}^2} 2\kappa_n \mathbf{m}_n^{\perp} \cdot \nabla m_n^{\parallel} d^2r \\ - \delta \sum_{n=1}^{N-1} \sum_{k=n+1}^{N} \int_{\mathbb{R}^2} \left(\mathbf{m}_n^{\perp} \cdot \nabla m_k^{\parallel} - \mathbf{m}_k^{\perp} \cdot \nabla m_n^{\parallel} \right) d^2r \\ - \delta \sum_{n=1}^{N} \sum_{k=1}^{N} \int_{\mathbb{R}^2} \int_{\mathbb{R}^2} \frac{\nabla m_n^{\parallel}(\mathbf{r}) \cdot \nabla m_k^{\parallel}(\mathbf{r}')}{4\pi|\mathbf{r} - \mathbf{r}'|} d^2r \; d^2r' \\ + \delta \sum_{n=1}^{N} \sum_{k=1}^{N} \int_{\mathbb{R}^2} \int_{\mathbb{R}^2} \frac{\nabla \cdot \mathbf{m}_n^{\perp}(\mathbf{r}) \nabla \cdot \mathbf{m}_k^{\perp}(\mathbf{r}')}{4\pi|\mathbf{r} - \mathbf{r}'|} d^2r \; d^2r', \end{aligned} \qquad (7)$$

where in the second and fourth lines of the right-hand side we carried out an integration by parts to rewrite the respective integrals (see [53]). Here

$$Q_n = Q_u + Q_n^{s,+} + Q_n^{s,-}, \qquad \kappa_n = \kappa_n^+ - \kappa_n^-, \qquad (8)$$

and the first line in the right-hand side of (7) contains the contributions of the intralayer exchange and effective perpendicular magnetic anisotropy that includes the local contribution of the intralayer demagnetizing field (shape anisotropy), the second line represents the DMI energy, and the rest of the terms are the additional $O(\delta)$ contributions to the stray field energy. In particular, the third line contains a stray field-mediated DMI-like term from the interplay between the volume and the surface charges in different layers that was identified in [39]. The fourth and the fifth lines in the right-hand side of (7) represent, respectively, the nonlocal contributions of the surface-surface and volume-volume charge interactions to the stray field energy.

III. THEORY OF ANTISYMMETRIC BILAYERS

We now turn our attention to the particular case of antisymmetric bilayers. For this system, we have $N = 2$, $Q_1 = Q_2 = Q > 1$ and $\kappa_1 = -\kappa_2 = \kappa \geq 0$, favoring a counter-clockwise rotation in the bottom layer and clockwise rotation in the top layer, with a flux closure-like arrangement of the magnetization in the two layers [39], see Fig. 1(a).

A. Thin film energy

The corresponding thin film energy is

$$\begin{aligned} E_2(\mathbf{m}_1, \mathbf{m}_2) = \sum_{n=1}^{2} \int_{\mathbb{R}^2} \left(|\nabla \mathbf{m}_n|^2 + (Q-1)|\mathbf{m}_n^{\perp}|^2 \right) d^2r \\ - 2\kappa \int_{\mathbb{R}^2} \left(\mathbf{m}_1^{\perp} \cdot \nabla m_1^{\parallel} - \mathbf{m}_2^{\perp} \cdot \nabla m_2^{\parallel} \right) d^2r \\ - \delta \int_{\mathbb{R}^2} \left(\mathbf{m}_1^{\perp} \cdot \nabla m_2^{\parallel} - \mathbf{m}_2^{\perp} \cdot \nabla m_1^{\parallel} \right) d^2r \\ - \delta \sum_{n=1}^{2} \sum_{k=1}^{2} \int_{\mathbb{R}^2} \int_{\mathbb{R}^2} \frac{\nabla m_n^{\parallel}(\mathbf{r}) \cdot \nabla m_k^{\parallel}(\mathbf{r}')}{4\pi|\mathbf{r} - \mathbf{r}'|} d^2r \, d^2r' \\ + \delta \sum_{n=1}^{2} \sum_{k=1}^{2} \int_{\mathbb{R}^2} \int_{\mathbb{R}^2} \frac{\nabla \cdot \mathbf{m}_n^{\perp}(\mathbf{r}) \nabla \cdot \mathbf{m}_k^{\perp}(\mathbf{r}')}{4\pi|\mathbf{r} - \mathbf{r}'|} d^2r \, d^2r'. \end{aligned} \qquad (9)$$

Notice that this energy is invariant with respect to the scaling transformation $\mathbf{r} \to \lambda \mathbf{r}$, provided that

$$Q - 1 \to \frac{Q-1}{\lambda^2}, \quad \kappa \to \frac{\kappa}{\lambda}, \quad \delta \to \frac{\delta}{\lambda}, \qquad (10)$$

which represents an important underlying scaling symmetry of the thin film energy. This allows us to eliminate one of the dimensionless parameters by introducing the new parameters

$$\bar{\delta} = \frac{\delta}{\sqrt{Q-1}}, \qquad \bar{\kappa} = \frac{\kappa}{\sqrt{Q-1}}, \qquad (11)$$

leading to the following simplified dimensionless energy

$$\begin{aligned}\bar{E}_2(\mathbf{m}_1, \mathbf{m}_2) = & \sum_{n=1}^{2} \int_{\mathbb{R}^2} \left(|\nabla \mathbf{m}_n|^2 + |\mathbf{m}_n^{\perp}|^2 \right) d^2r \\ & - 2\bar{\kappa} \int_{\mathbb{R}^2} \left(\mathbf{m}_1^{\perp} \cdot \nabla m_1^{\parallel} - \mathbf{m}_2^{\perp} \cdot \nabla m_2^{\parallel} \right) d^2r \\ & - \bar{\delta} \int_{\mathbb{R}^2} \left(\mathbf{m}_1^{\perp} \cdot \nabla m_2^{\parallel} - \mathbf{m}_2^{\perp} \cdot \nabla m_1^{\parallel} \right) d^2r \\ & - \bar{\delta} \sum_{n=1}^{2} \sum_{k=1}^{2} \int_{\mathbb{R}^2} \int_{\mathbb{R}^2} \frac{\nabla m_n^{\parallel}(\mathbf{r}) \cdot \nabla m_k^{\parallel}(\mathbf{r}')}{4\pi |\mathbf{r} - \mathbf{r}'|} \, d^2r \, d^2r' \\ & + \bar{\delta} \sum_{n=1}^{2} \sum_{k=1}^{2} \int_{\mathbb{R}^2} \int_{\mathbb{R}^2} \frac{\nabla \cdot \mathbf{m}_n^{\perp}(\mathbf{r}) \nabla \cdot \mathbf{m}_k^{\perp}(\mathbf{r}')}{4\pi |\mathbf{r} - \mathbf{r}'|} \, d^2r \, d^2r', \end{aligned} \tag{12}$$

that satisfies $E_2(\mathbf{m}_1, \mathbf{m}_2) = \bar{E}_2(\bar{\mathbf{m}}_1, \bar{\mathbf{m}}_2)$, where $\bar{\mathbf{m}}_n(\mathbf{r}) = \mathbf{m}_n(\mathbf{r}/\sqrt{Q-1})$. In other words, $\bar{E}_2$ gives the energy of the normalized magnetization configuration $(\mathbf{m}_1, \mathbf{m}_2)$ in the two layers, with lengths measured in the units of the Bloch wall thickness $L_B = \ell_{ex}/\sqrt{Q-1}$. The behavior of the energy $\bar{E}_2$ is completely determined by only two dimensionless parameters: $\bar{\kappa}$ and $\bar{\delta}$.

B. Antisymmetric profiles

To better understand the behavior of the critical points of the energy in (12), we consider an ansatz in which the in-plane components of the magnetization in the two layers are anti-parallel, while the out-of-plane components are parallel. Setting

$$\mathbf{m}_1 = (\mathbf{m}^{\perp}, m^{\parallel}), \qquad \mathbf{m}_2 = (-\mathbf{m}^{\perp}, m^{\parallel}), \tag{13}$$

for $\mathbf{m} = (\mathbf{m}^{\perp}, m^{\parallel})$ leads to $\bar{E}_2(\mathbf{m}_1, \mathbf{m}_2) = 2\bar{E}^{\pm}(\mathbf{m})$, where

$$\begin{aligned}\bar{E}^{\pm}(\mathbf{m}) = & \\ & \int_{\mathbb{R}^2} \left(|\nabla \mathbf{m}|^2 + |\mathbf{m}^{\perp}|^2 - (2\bar{\kappa} + \bar{\delta}) \mathbf{m}^{\perp} \cdot \nabla m^{\parallel} \right) d^2r \\ & - 2\bar{\delta} \int_{\mathbb{R}^2} \int_{\mathbb{R}^2} \frac{\nabla m^{\parallel}(\mathbf{r}) \cdot \nabla m^{\parallel}(\mathbf{r}')}{4\pi |\mathbf{r} - \mathbf{r}'|} \, d^2r \, d^2r'. \end{aligned} \tag{14}$$

This ansatz is motivated by the energetic advantages it provides: in a skyrmion profile the DMI and the surface-volume charge interactions of both layers cooperate, while the energy penalty due to the volume-volume charge interactions cancels out. In particular, the ansatz has been rigorously shown to be valid in the conformal limit for $\bar{\kappa} = 0$ [39] and is confirmed by the numerical simulations for the parameter ranges at which the skyrmion solutions are observed (see Sec. III G).

C. Bilayer skyrmions

The expression in (14) coincides with the energy of a single ferromagnetic layer of thickness $2\bar{\delta}$ with the effective DMI constant $\bar{\kappa} + \frac{1}{2}\bar{\delta}$, in which the volume-volume charge interaction penalty term is absent. One can easily adapt the proof of existence of skyrmion solutions as local energy minimizers with topological degree $q(\mathbf{m}) = 1$, where

$$q(\mathbf{m}) = \frac{1}{4\pi} \int_{\mathbb{R}^2} \mathbf{m} \cdot (\partial_x \mathbf{m} \times \partial_y \mathbf{m}) \, d^2r \tag{15}$$

defines the Brouwer degree of a map $\mathbf{m} : \mathbb{R}^2 \to \mathbb{S}^2$, with the convention that $\mathbf{m}(\infty) = -\hat{\mathbf{z}}$ [54, 55]. More precisely, we have the following existence result.

Theorem 1. *Let* $\bar{\delta} \geq 0$ *and* $\bar{\kappa} \geq 0$ *be such that*

$$0 < 2\bar{\kappa} + 3\bar{\delta} \leq \sqrt{2}. \tag{16}$$

Then there exists a minimizer of $\bar{E}^{\pm}$ *among all* $\mathbf{m} \in H^1_{\mathrm{loc}}(\mathbb{R}^2; \mathbb{S}^2)$ *such that* $q(\mathbf{m}) = 1$, $\int_{\mathbb{R}^2} |\nabla \mathbf{m}|^2 d^2r < 16\pi$, *and* $\mathbf{m} + \hat{\mathbf{z}} \in L^2(\mathbb{R}^2; \mathbb{R}^3)$.

As was already mentioned, the asymptotic behavior of these solutions in the absence of the DMI, $\bar{\kappa} = 0$, and in the conformal limit $\bar{\delta} \to 0$ has been explicitly identified in [39, Theorem 2]. This result may be straightforwardly extended to the case of $\bar{\kappa} > 0$ tending jointly to zero, yielding the following expression for the dimensionless radius $\bar{\rho}_2^{\mathrm{sky}}$ of the skyrmion in an antisymmetric bilayer:

$$\bar{\rho}_2^{\mathrm{sky}} \simeq \frac{32\bar{\kappa} + (16 + \pi^2)\bar{\delta}}{-64 W_{-1}\left(-\frac{32\bar{\kappa} + (16+\pi^2)\bar{\delta}}{128} e^{1+\gamma} \right)}, \tag{17}$$

where $\gamma \approx 0.5772$ is the Euler-Mascheroni constant and $W_{-1}(t)$ is the Lambert W function [56], while the skyrmion energy satisfies

$$\begin{aligned}\bar{E}_2^{\mathrm{sky}} \simeq & \, 16\pi \\ & - \frac{\pi \bar{\rho}_2^{\mathrm{sky}}}{4} \left(32\bar{\kappa} + (16 + \pi^2)\bar{\delta} - 32\bar{\rho}_2^{\mathrm{sky}} \right). \end{aligned} \tag{18}$$

The above two formulas are valid for $0 < \bar{\kappa} + \bar{\delta} \ll 1$. The solutions are asymptotically radial, satisfy (13) as minimizers of (12) (as follows from the argument in [39]), and are conjectured to be such for all values of the parameters.

D. Skyrmion bursting

We now investigate the range of existence of the above solutions as the values of $\bar{\kappa}$ and $\bar{\delta}$ are increased beyond the range covered by Theorem 1. Assuming radial symmetry, for $\bar{\delta} = 0$ such an analysis was performed in [57], where it was shown, using formal asymptotic analysis and numerical simulations, that as $\bar{\kappa}$ approaches the critical value $\bar{\kappa}_c = 4/\pi$ from below, the skyrmion solution transforms into a bubble-like profile $\mathbf{m} = \mathbf{m}_{\bar{\rho}}$, where

$$\mathbf{m}_{\bar{\rho}}(\mathbf{r}) \simeq \left(-\frac{\mathbf{r}}{|\mathbf{r}|} \operatorname{sech}(|\mathbf{r}| - \bar{\rho}), \tanh(\bar{\rho} - |\mathbf{r}|) \right), \tag{19}$$

whose radius $\bar{\rho}$ is determined by the value of $\bar{\kappa}$ and diverges as $\bar{\kappa} \to \bar{\kappa}_c$. The analysis of [57] yields $\bar{\rho} \simeq \sqrt{\frac{c\bar{\kappa}_c}{2(\bar{\kappa}_c - \bar{\kappa})}}$, with the constant $c \approx 0.9605$ determined numerically. Nevertheless, as was already pointed out in [57], this radius may be obtained with a very good accuracy (yielding $c = 1$ above) by plugging in the ansatz in (19) into the energy and calculating its local maximum in $\bar{\rho}$ to the leading order in $\bar{\rho} \gg 1$, as was done in [58]. Below we use the same approximation in the presence of the non-local terms in the energy to investigate the behavior of solutions for $\bar{\kappa} \sim \bar{\kappa}_c$ and $\bar{\delta} > 0$.

Substituting the ansatz in (19) into the energy in (14) and calculating the stray field energy in Appendix A, we obtain

$$\bar{E}^{\pm}(\mathbf{m}_{\bar{\rho}}) \simeq 2\pi\bar{\rho}\left[4 - \pi(\bar{\kappa} + \tfrac{1}{2}\bar{\delta})\right] + \frac{4\pi}{\bar{\rho}} - 8\bar{\delta}\bar{\rho}\ln\left(\frac{8\bar{\rho}}{\pi}e^{\gamma-1}\right), \tag{20}$$

to the leading order in $\bar{\rho} \gg 1$, with relative errors of algebraic order in $1/\bar{\rho}$. In this expression, the first term is the domain wall energy for the bubble of radius $\bar{\rho}$, the second term is an additional exchange energy contribution from the angular gradient of the magnetization [58], and the last term is the contribution of surface-surface charge interaction. This expression may be analyzed as a function of $\bar{\rho}$, yielding two critical points for $\bar{\kappa} < \bar{\kappa}_2^b(\bar{\delta})$, one critical point for $\bar{\kappa} = \bar{\kappa}_2^b(\bar{\delta})$, or no critical points, for $\bar{\kappa} > \bar{\kappa}_2^b(\bar{\delta})$, for any fixed $\bar{\delta} > 0$ (see Fig. 2). The borderline case of one critical point occurs at the inflection point of the energy $\bar{E}^{\pm}(\mathbf{m}_{\bar{\rho}})$ as a function of $\bar{\rho}$ given by $\bar{\rho} = \bar{\rho}_2^b = \left(\pi/\bar{\delta}\right)^{1/2}$. A simple calculation then shows that

$$\bar{\kappa}_2^b \simeq \frac{4}{\pi} - \frac{2\bar{\delta}}{\pi^2}\left[\ln\left(\frac{64}{\pi\bar{\delta}}\right) + 1 + 2\gamma + \frac{\pi^2}{4}\right]. \tag{21}$$

This formula is expected to be accurate for $\bar{\delta} \lesssim 1$, corresponding to our assumption $\bar{\rho} \gtrsim 1$, and gives the predicted transition between the parameter region where $\bar{\kappa} < \bar{\kappa}_2^b(\bar{\delta})$, for which a local minimum of the energy $\bar{E}^{\pm}(\mathbf{m}_{\bar{\rho}})$ exists, and a region where $\bar{\kappa} > \bar{\kappa}_2^b(\bar{\delta})$, for which no local minimum exists and the energy is monotonically decreasing in $\bar{\rho}$. Thus, the value of $\bar{\kappa}_2^b$ may be associated with a bursting line for the skyrmion solution in antisymmetric ferromagnetic bilayers, with the bursting radius $\bar{\rho}_2^b$.

E. Thermal stability

We now turn to the characterization of thermal stability of the skyrmion solutions for $\bar{\delta} > 0$ and $0 < \bar{\kappa} < \bar{\kappa}_2^b(\bar{\delta})$. Note that due to its topological protection, a skyrmion may not continuously transform into the uniformly magnetized ferromagnetic state. Nevertheless, as we argued in [59], a skyrmion may disappear discontinuously as a result of a singularity formation (at the continuum level) leading to skyrmion collapse (see also [10, 11, 54, 60, 61]). The energy cost of such a barrier-crossing event is determined by the transition state in the form of a "zero-radius" skyrmion, which is equal to the minimal value of the exchange energy in the considered topological class. In the case of the antisymmetric bilayers with the ansatz in (13) this results in the collapse barrier

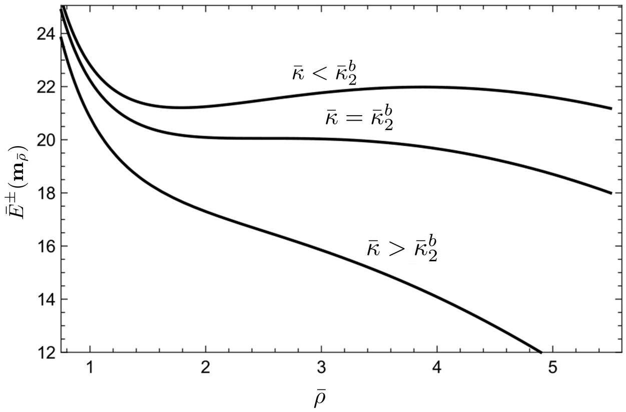

FIG. 2. The dependence of $\bar{E}^{\pm}(\mathbf{m}_{\bar{\rho}})$ from (20) on $\bar{\rho}$ for $\bar{\delta} = 0.5$ and $\bar{\kappa} = 0.4$, $\bar{\kappa} = 0.4293$, and $\bar{\kappa} = 0.5$, respectively.

$$\Delta\bar{E}_2^{c,0} = 16\pi - 2\bar{E}^{\pm}(\mathbf{m}^{\text{sky}}), \tag{22}$$

where $\mathbf{m}^{\text{sky}}$ is the profile that locally minimizes $\bar{E}^{\pm}$ among all $\mathbf{m} : \mathbb{R}^2 \to \mathbb{S}^2$ with $q(\mathbf{m}) = 1$ and $\mathbf{m}(\infty) = -\hat{\mathbf{z}}$.

At the same time, in the presence of the non-local effects due to stray field another scenario is possible, in which the skyrmion radius grows under the action of thermal noise, reaching the saddle point solution corresponding to the largest critical point of the energy in (20) for $\bar{\rho} > \bar{\rho}_2^b$. When $\bar{\kappa}$ is not in the immediate vicinity of $\bar{\kappa}_c$ and $\bar{\delta} > 0$ is sufficiently small, we can drop the $4\pi/\bar{\rho}$ term from the energy in (20) and calculate that the saddle point solution corresponds to the radius $\bar{\rho} = \bar{\rho}_2^{\text{sad}}$, where

$$\bar{\rho}_2^{\text{sad}} \simeq \frac{\pi}{8}\exp\left(\frac{\pi}{\bar{\delta}} - \frac{\pi^2\bar{\kappa}}{4\bar{\delta}} - \frac{\pi^2}{8} - \gamma\right). \tag{23}$$

The associated energy barrier is

$$\Delta\bar{E}_2^{b,0} = 2\bar{E}^{\pm}(\mathbf{m}_{\bar{\rho}_2^{\text{sad}}}) - 2\bar{E}^{\pm}(\mathbf{m}^{\text{sky}}), \tag{24}$$

where

$$\bar{E}^{\pm}(\mathbf{m}_{\bar{\rho}_2^{\text{sad}}}) \simeq \pi\bar{\delta}\exp\left(\frac{\pi}{\bar{\delta}} - \frac{\pi^2\bar{\kappa}}{4\bar{\delta}} - \gamma - \frac{\pi^2}{8}\right). \tag{25}$$

These formulas are expected to be asymptotically exact for $0 \leq \bar{\kappa} < \bar{\kappa}_c$ as $\bar{\delta} \to 0$.

Comparing the two energy barriers, one can see that the most likely thermally activated event (under the ansatz in (13) and the radiality assumption) would be determined by the minimum value of the two barriers above, and the skyrmion lifetime in the Arrhenius regime will, therefore, be given by

$$\tau = \tau_0 \exp\left(\frac{Ad}{k_B T}\,\Delta\bar{E}_2\right), \tag{26}$$

where $\Delta\bar{E}_2 = \min(\Delta\bar{E}_2^{c,0}, \Delta\bar{E}_2^{b,0})$, k_B is the Boltzmann constant, T is temperature, and τ_0 is the characteristic attempt timescale. It is thus possible to maximize the lifetime by choosing the parameters of the problem for which the two barriers above coincide, which amounts to setting

$$\bar{E}^{\pm}(\mathbf{m}_{\bar{\rho}_2^{\mathrm{sad}}}) = 8\pi. \tag{27}$$

This yields the predicted optimal value $\bar{\kappa} = \bar{\kappa}_2^{\mathrm{opt}}$ of the dimensionless DMI strength

$$\bar{\kappa}_2^{\mathrm{opt}} \simeq \frac{4}{\pi} - \frac{4\bar{\delta}}{\pi^2}\left[\ln\left(\frac{8}{\bar{\delta}}\right) + \gamma + \frac{\pi^2}{8}\right], \tag{28}$$

for fixed $\bar{\delta} > 0$. Once again, this formula is expected to be accurate for $\bar{\delta} \lesssim 1$, yielding $\bar{\rho}_2^{\mathrm{sad}} \gtrsim 1$.

We wish to point out, however, that in reality the determination of the barrier-crossing events in the case of bilayers is more challenging due to the fact that the assumption of antisymmetry in (13) used to derive the above simple expressions may not be the most favorable for the transition states. More specifically, the collapse barrier should not require that the skyrmions in both layers collapse simultaneously, as the more energetically favorable scenario should be the collapse in only one layer. Thus, the value of 16π in (22) should be replaced with $8\pi + \bar{E}_2(\mathbf{m}_1^{\mathrm{sky1}}, \mathbf{m}_2^{\mathrm{sky1}})$, where 8π is the energy of the zero-radius skyrmion in one layer and $(\mathbf{m}_1^{\mathrm{sky1}}, \mathbf{m}_2^{\mathrm{sky1}})$ is the locally energy minimizing configuration for $\bar{E}_2(\mathbf{m}_1, \mathbf{m}_2)$ with $q(\mathbf{m}_1) = 1$ and $q(\mathbf{m}_2) = 0$, i.e., the configuration with a skyrmion in only one layer. Here the fact that the topologically non-trivial profile is assumed to be in the first layer is not essential, since the energy $\bar{E}_2(\mathbf{m}_1, \mathbf{m}_2)$ enjoys a symmetry with respect to swapping the two layers, provided that the sign of the in-plane components is reversed, i.e., we have $\bar{E}_2(\mathbf{m}_1, \mathbf{m}_2) = \bar{E}_2(\tilde{\mathbf{m}}_1, \tilde{\mathbf{m}}_2)$, where $\tilde{\mathbf{m}}_{1,2} = (-\mathbf{m}_{2,1}^{\perp}, m_{2,1}^{\parallel})$. Hence, the collapse barrier should rather be

$$\Delta\bar{E}_2^{c} = 8\pi + \bar{E}_2(\mathbf{m}_1^{\mathrm{sky1}}, \mathbf{m}_2^{\mathrm{sky1}}) - \bar{E}_2(\mathbf{m}_1^{\mathrm{sky2}}, \mathbf{m}_2^{\mathrm{sky2}}), \tag{29}$$

where $(\mathbf{m}_1^{\mathrm{sky2}}, \mathbf{m}_2^{\mathrm{sky2}})$ is the locally energy minimizing configuration for $\bar{E}_2(\mathbf{m}_1, \mathbf{m}_2)$ with $q(\mathbf{m}_1) = q(\mathbf{m}_2) = 1$, i.e., the configuration with a skyrmion in both layers. Analogously, the bursting barrier is a priori given by

$$\Delta\bar{E}_2^{b} = \bar{E}_2(\mathbf{m}_1^{\mathrm{sad2}}, \mathbf{m}_2^{\mathrm{sad2}}) - \bar{E}_2(\mathbf{m}_1^{\mathrm{sky2}}, \mathbf{m}_2^{\mathrm{sky2}}), \tag{30}$$

where $(\mathbf{m}_1^{\mathrm{sad2}}, \mathbf{m}_2^{\mathrm{sad2}})$ is the lowest energy saddle point configuration with $q(\mathbf{m}_1^{\mathrm{sad2}}) = q(\mathbf{m}_2^{\mathrm{sad2}}) = 1$ connecting the skyrmion configuration $(\mathbf{m}_1^{\mathrm{sky2}}, \mathbf{m}_2^{\mathrm{sky2}})$ with the striped-out state via gradient descent.

In practice, the barriers with or without the antisymmetry ansatz in (13) are expected to be close to one another, as both the locally energy minimizing configuration $(\mathbf{m}_1^{\mathrm{sky2}}, \mathbf{m}_2^{\mathrm{sky2}})$ with skyrmions in both layers and the lowest energy saddle point configuration $(\mathbf{m}_1^{\mathrm{sad2}}, \mathbf{m}_2^{\mathrm{sad2}})$ are expected to obey (13), while the energy of $(\mathbf{m}_1^{\mathrm{sky1}}, \mathbf{m}_2^{\mathrm{sky1}})$ for the parameters of optimal stability of $(\mathbf{m}_1^{\mathrm{sky2}}, \mathbf{m}_2^{\mathrm{sky2}})$ should be close to that of the zero-radius skyrmion, i.e., one expects $\bar{E}_2(\mathbf{m}_1^{\mathrm{sky1}}, \mathbf{m}_2^{\mathrm{sky1}}) \simeq 8\pi$ for most of the relevant parameters (see also Sec. III G).

F. Beyond bursting

As bursting of a skyrmion is expected to lead to the formation and growth of a skyrmionic bubble followed by stripe-out, it is also instructive to calculate the period of the resulting ground state periodic stripe configuration corresponding to the demagnetizing state in the considered system. This can be done exactly as in [62], and with a few straightforward modifications we obtain that the energy density per unit area (in the units of Ad/L_B^2) of a periodic stripe configuration $\mathbf{m}_{\bar{L}}^{\mathrm{stripe}}$ with period $\bar{L}$ (in the units of L_B) in one layer is given by

$$\begin{aligned}\frac{2\bar{E}^{\pm}(\mathbf{m}_{\bar{L}}^{\mathrm{stripe}})}{\bar{L}^2} \simeq{}& \frac{4}{\bar{L}}\left[4 - \pi(\bar{\kappa} + \tfrac{1}{2}\bar{\delta})\right] \\ &- \frac{16\bar{\delta}}{\pi\bar{L}}\left[\ln\left(\frac{\bar{L}}{\pi^2}\right) + \gamma + 1\right],\end{aligned} \tag{31}$$

where we assumed that the configuration in the two layers satisfies (13) with $\mathbf{m} = \mathbf{m}_{\bar{L}}^{\mathrm{stripe}}$. Minimizing this expression with respect to $\bar{L}$ yields the optimal stripe period

$$\bar{L}_2^{\mathrm{opt}} \simeq \pi^2 \exp\left(\frac{\pi}{\bar{\delta}} - \frac{\pi^2\bar{\kappa}}{4\bar{\delta}} - \frac{\pi^2}{8} - \gamma\right). \tag{32}$$

Again, these formulas are expected to be asymptotically exact for $0 \leq \bar{\kappa} < \bar{\kappa}_c$ as $\bar{\delta} \to 0$.

Comparing the diameter of the saddle point solution obtained in Sec. III E and the equilibrium width of a single stripe, we see that their ratio reaches a universal value:

$$\frac{2\bar{\rho}_2^{\mathrm{sad}}}{\frac{1}{2}\bar{L}_2^{\mathrm{opt}}} \simeq \frac{1}{2\pi} \approx 0.1592 \tag{33}$$

for $\bar{\delta} \ll 1$ and $\bar{\kappa}$ not too close to $\bar{\kappa}_c$. Thus, there should be a fairly well-defined range of radial growth of the skyrmionic bubble after bursting caused by thermal fluctuations before it undergoes a stripe-out instability. This is indeed observed numerically in sufficiently large computational domains upon skyrmion bursting.

G. Numerical skyrmion solutions and energy barriers

We now perform a numerical construction of skyrmion solutions as local energy minimizers in the $(\bar{\kappa}, \bar{\delta})$ plane by carrying out micromagnetic simulations of the antisymmetric bilayer system, using the Mumax3 software [51]. For that purpose, we consider two adjacent exchange-decoupled ferromagnetic layers of thickness $d = 1$ nm and fix the parameters of the magnetic material to have the characteristic values for transition metal ultrathin ferromagnetic layers such as Pt/Co/AlO$_x$ with $A = 20$ pJ/m and $M_s = 1$ MA/m [63, 64]. This yields the exchange length $\ell_{ex} \approx 5.64$ nm. We next vary the DMI strength $D = D^{s,+}/d$ (in the units of J/m^2, conventionally normalized per unit volume), setting the DMI constant in the bottom layer to D and the DMI constant in the top layer to $-D$, respectively, as well as the anisotropy constant K_u, in such a way as to express the results in terms of the dimensionless quantities $\bar{\kappa}$ and $\bar{\delta}$ defined in (11). As the system is within the validity range of the thin film model of Sec. II, $d \ll \ell_{ex}$, the dimensionless results thus obtained depend only weakly on the specific choices of the dimensional parameters.

For a given pair $(\bar{\kappa}, \bar{\delta})$ we thus choose

$$K_u = K_d \left(1 + \frac{d^2}{\ell_{ex}^2 \bar{\delta}^2}\right), \qquad D = \frac{d K_d \bar{\kappa}}{\bar{\delta}}. \tag{34}$$

The computational domain is discretized, using a $2048 \times 2048 \times 2$ grid with the discretization steps $(\Delta x, \Delta y, \Delta z)$ in the (X, Y, Z) directions set to $\Delta x = \Delta y = 0.3$ nm and $\Delta z = 1$ nm. Periodic boundary conditions in the plane are implemented by specifying the number of repeats in (X, Y, Z) to be $(5, 5, 0)$. The exchange is active only in the (X, Y) directions.

Using the parametrization in (34), we carried out a parameter sweep in the $(\bar{\kappa}, \bar{\delta})$ plane with a grid spanning $0.05 \leq \bar{\delta} \leq 0.75$ with increments of $\Delta\bar{\delta} = 0.025$, and $0.01 \leq \bar{\kappa} \leq 1.26$ with increments of $\Delta\bar{\kappa} = 0.025$. The maximum value of $\bar{\kappa}$ is slightly below $\bar{\kappa}_c$, while the maximum value of $\bar{\delta}$ corresponds approximately to the expected value of skyrmion bursting threshold given by (21) at $\bar{\kappa} = 0$. To carry out this sweep efficiently, we first initialize the system with an antisymmetric Néel skyrmion configuration for $\bar{\delta} = 0.05$ and $\bar{\kappa} = 1.1337$ on the $\bar{\kappa} = \bar{\kappa}_2^b(\bar{\delta})$ curve obtained by running the `minimize` routine with an identical Bloch skyrmion-like initial condition of radius 5 nm in both layers to convergence. We then march this configuration along the $\bar{\kappa} = \bar{\kappa}_2^{\text{opt}}(\bar{\delta})$ curve by increasing $\bar{\delta}$ stepwise along the grid and then running the `minimize` routine to obtain the skyrmion configurations for $\bar{\kappa} = \bar{\kappa}_2^{\text{opt}}(\bar{\delta})$ to convergence. We note that this curve corresponds to the optimal stability of the skyrmion solution, and we observe, as expected, that the numerical convergence to the skyrmion profile in the vicinity of this optimal line is very fast. We finally use the obtained profiles at a given $\bar{\delta}$ and $\bar{\kappa} = \bar{\kappa}_2^{\text{opt}}(\bar{\delta})$ as initial seeds to sweep down and up the values of $\bar{\kappa}$ along the grid and repeat the procedure for each grid point in $\bar{\delta}$.

Next, to calculate the skyrmion collapse energy barrier defined in (29) we repeated the procedure to compute the single layer skyrmion solutions $(\mathbf{m}_1^{\text{sky1}}, \mathbf{m}_2^{\text{sky1}})$ with an initial seed in the form of a skyrmion in only one layer, obtaining a family of Néel skyrmions in only one layer coupled magnetostatically to a nearly uniformly magnetized state in the other layer. We then extracted the energy $\bar{E}_2(\mathbf{m}_1^{\text{sky1}}, \mathbf{m}_2^{\text{sky1}})$ of these configurations, setting it to the last obtained value if such a solution numerically collapsed upon decrease of $\bar{\kappa}$ at fixed $\bar{\delta}$ in the course of the simulation. Using (29), we then calculated the collapse barrier $\Delta\bar{E}_2^c$ in the parameter region in which the antisymmetric Néel skyrmion solution $(\mathbf{m}_1^{\text{sky2}}, \mathbf{m}_2^{\text{sky2}})$ was computed.

The results of the above simulations in dimensionless form are summarized in Fig. 3, where the simulation data have been linearly interpolated between the grid points. Figure 3(a) shows the skyrmion radius $\bar{\rho}_2^{\text{sky}}$ in the units of $L_B = \sqrt{A/(K_u - K_d)}$ (which varies from point to point) defined as the radius of the zero level set of $m_{1,2}^{\|}$ from the converged solution $(\mathbf{m}_1^{\text{sky2}}, \mathbf{m}_2^{\text{sky2}})$. Figure 3(b) shows the skyrmion energy $\bar{E}_2^{\text{sky}}$ in the units of Ad defined as the difference between the total energy of the system and the energy of the uniformly magnetized state. In all the simulations the resulting skyrmion profiles were found to obey (13) and be radially symmetric. The skyrmion solutions in Figs. 3(a) and 3(b) exhibit radii that increase with increasing $\bar{\kappa}$ or $\bar{\delta}$, and energies that decrease with increasing $\bar{\kappa}$ or $\bar{\delta}$. In addition, the lines of constant radii and energies extend over a wide range of $\bar{\kappa}$ and $\bar{\delta}$ values. We also observe that for sufficiently low $\bar{\kappa}$ and/or $\bar{\delta}$ there is no numerical solution due to numerical collapse at fixed finite discretization in the film plane. This is due to the numerics being unable to resolve the vanishing skyrmion radius as $\bar{\kappa}, \bar{\delta} \to 0$, see (17). Note, however, that mathematically the skyrmion solutions continue to exist for all sufficiently small values of $\bar{\kappa}$ and $\bar{\delta}$, as is guaranteed by Theorem 1. These solutions can be obtained numerically by reducing the discretization step Δx. In contrast, at high $\bar{\kappa}$ or $\bar{\delta}$ the numerical solution bursts into a bubble occupying half of the computational domain, with bursting occurring as predicted in Sec. III D. We exclude these solutions from the dataset. We note a very good quantitative agreement between this numerical bursting and the predicted busting line defined in Eq.(21) and represented by a dashed line in Figs. 3(a)-(e).

Figure 3(c) shows the plot of the bilayer collapse barrier $\Delta\bar{E}_2^c$. It increases from zero at low values of $\bar{\kappa}$ and $\bar{\delta}$ and reaches its maximum at $\bar{\kappa} = \bar{\kappa}_2^b(\bar{\delta})$ for each $\bar{\delta}$. The maximum value of $\Delta\bar{E}_2^c$ at $\bar{\kappa} = \kappa_2^b(\bar{\delta})$ increases with decreasing $\bar{\delta}$ and reaches the asymptotic value of $\Delta\bar{E}_2^c = 8\pi$ as $\bar{\delta} \to 0$ and $\bar{\kappa} \to \bar{\kappa}_c$, corresponding to two decoupled ferromagnetic layers. We note that since $\bar{E}_2(\mathbf{m}_1^{\text{sky1}}, \mathbf{m}_2^{\text{sky1}}) < 8\pi$, the energy of a "zero-

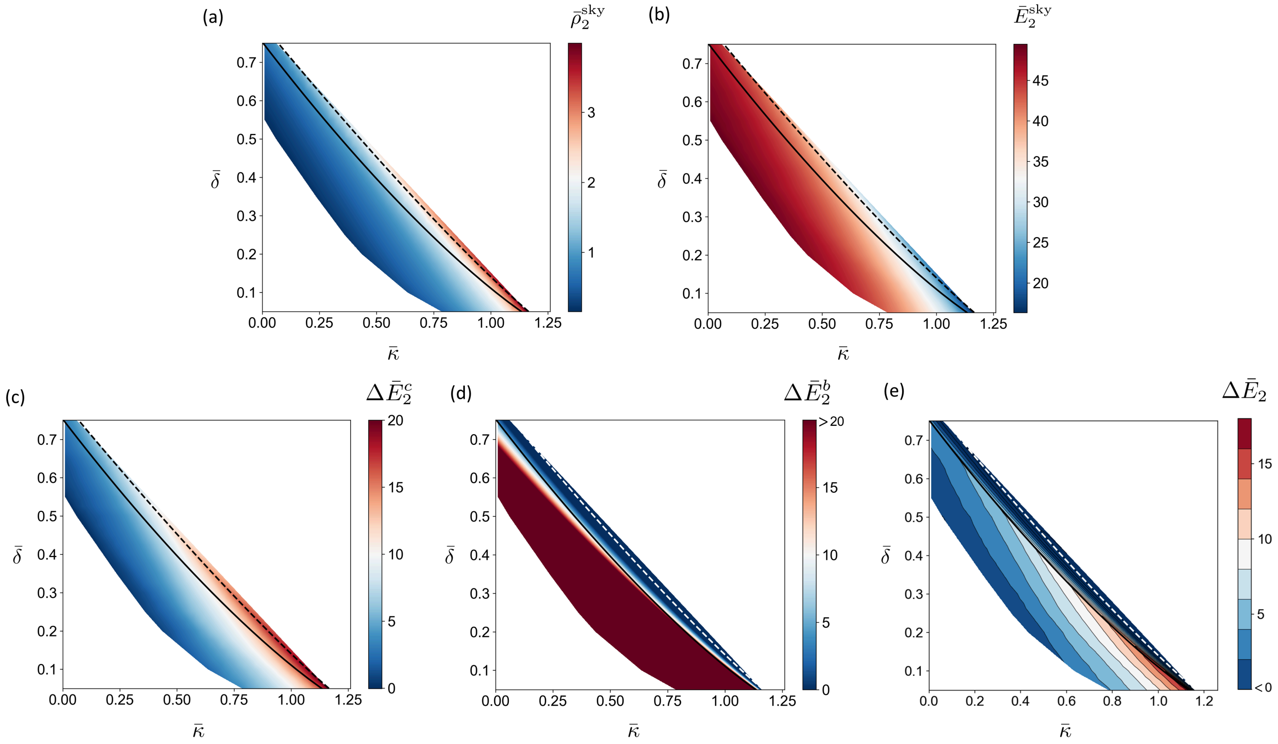

FIG. 3. Summary of the numerical results obtained from Mumax3 simulations (see Sec.III G for details) of an antisymmetric ferromagnetic bilayer with $A = 20$ J/m, $M_s = 10^6$ A/m, $d = 1$ nm, and K_u and D varied in accordance with (34) on a 614.4×614.4 nm computational domain with periodic boundary conditions in the plane: (a) the dimensionless radius $\bar{\rho}_2^{\rm sky}$; (b) the dimensionless skyrmion energy $\bar{E}_2^{\rm sky}$; (c) the dimensionless collapse energy barrier $\Delta\bar{E}_2^c$; (d) the dimensionless bursting energy barrier $\Delta\bar{E}_2^b$; (e) the dimensionless effective energy barrier $\Delta\bar{E}_2$. The solid line shows $\bar{\kappa}_2^{\rm opt}(\bar{\delta})$ and the dashed line shows $\bar{\kappa}_2^b(\bar{\delta})$ governed, respectively, by (28) and (21).

radius" skyrmion in a single layer, the collapse barrier $\Delta\bar{E}_2^c$ defined in (29) is smaller than $\Delta\bar{E}_2^{c,0}$ from (22). Therefore, by the definition of $\bar{\kappa}_2^{\rm opt}$ [see (27)], the value of the bursting energy barrier $\Delta\bar{E}_2^{b,0}$ predicted in (24) is greater than $\Delta\bar{E}_2^c$ for all $\bar{\kappa} \leq \bar{\kappa}_2^{\rm opt}(\bar{\delta})$ for a given $\bar{\delta}$. Thus, one expects bursting to be active only in the narrow range $\bar{\kappa}_2^{\rm opt}(\bar{\delta}) \leq \bar{\kappa} \leq \bar{\kappa}_2^b(\bar{\delta})$ for each $\bar{\delta}$. This is indeed what is observed in Fig. 3(d), which shows the bursting barrier from (30) as a function of $\bar{\kappa}$ and $\bar{\delta}$, where $\bar{E}_2(\mathbf{m}_1^{\rm sad}, \mathbf{m}_2^{\rm sad}) \simeq 2\bar{E}^{\pm}(\mathbf{m}_{\bar{\rho}_2^{\rm sad}})$ is the approximate saddle point energy from (25) and $\bar{E}_2(\mathbf{m}_1^{\rm sky2}, \mathbf{m}_2^{\rm sky2})$ is the skyrmion energy obtained numerically, all in the units of Ad [we set $\Delta\bar{E}_2^b = 0$ when the above definition yields a negative value, indicating the breakdown of validity of (25)]. As expected, the bursting barrier exceeds the value of $\Delta\bar{E}_2^c$ to the left of the $\bar{\kappa} = \bar{\kappa}_2^{\rm opt}(\bar{\delta})$ curve, but very quickly drops off to zero as $\bar{\kappa}$ approaches $\bar{\kappa}_2^b(\bar{\delta})$. Thus, the optimal thermal stability of a skyrmion indeed occurs at $\bar{\kappa} \simeq \bar{\kappa}_2^{\rm opt}(\bar{\delta})$ for every fixed $\bar{\delta}$. This is illustrated in Fig. 3(e), which shows the effective energy barrier $\Delta\bar{E}_2 = \min(\Delta\bar{E}_2^c, \Delta\bar{E}_2^b)$. In Fig. 3(e), we see that below the curve $\bar{\kappa} = \bar{\kappa}_2^{\rm opt}(\bar{\delta})$ the lines of equal effective energy barrier $\Delta\bar{E}_2$ again cover a wide range of $\bar{\kappa}$ and $\bar{\delta}$ values. This highlights the existence of two degrees of freedom, $\bar{\kappa}$ and $\bar{\delta}$, for the optimization of skyrmion stability in the antisymmetric bilayer system. It is a clear confirmation that in this system the stray field plays an important stabilizing role via the surface-volume charge interactions, cooperating with the DMI, as could be inferred by looking at the skyrmion energy in (14).

IV. COMPARISON WITH SYNTHETIC ANTIFERROMAGNETS AND FERROMAGNETIC MONOLAYERS

In order to emphasize the potential advantages of the antisymmetric bilayer over other systems, we compare it with the typical layer stacks for skyrmion applications, represented in Figs. 1(b) and 1(c), namely, SAF and ferromagnetic monolayers. We start by presenting the models and comparatively discussing the numerical skyrmion solutions for the case of SAF in Sec. IV A and ferromagnetic monolayers in Sec. IV B, respectively. Finally, in Section IV C we apply our predictions to the family of prototypical spintronic materials, the Pt/Co/AlO$_x$ stacks [63, 65, 66]. The radii and effective energy barriers for skyrmions in an antisymmetric bilayer, SAF and a monolayer constructed with this material as a building block are given as a function of dimensional thickness and interfacial DMI, and then compared to one another.

A. Synthetic antiferromagnet

As was already mentioned, SAF multilayers are among the most promising systems to achieve room temperature stable magnetic skyrmions. They consist of a basic unit in which two identical ferromagnetic monolayers with the DMI of the same sign in each layer are strongly antiferromagnetically coupled, leading effectively to a cancellation of the non-local magnetostatic interactions. Such an additional interlayer coupling may be easily incorporated into our modeling framework, amounting to an additional term in the micromagnetic energy in (2) [45, 67]:

$$\begin{aligned}\mathcal{E}_J(\mathbf{M}) &= \mathcal{E}(\mathbf{M}) \\ &\quad - \frac{J}{M_s^2}\sum_{n=1}^{N-1}\int_{\mathbb{R}^2}\Big(\mathbf{M}_n^+\cdot\mathbf{M}_{n+1}^- - \mathbf{M}_n^\infty\cdot\mathbf{M}_{n+1}^\infty\Big)d^2r,\end{aligned} \tag{35}$$

where J is the interlayer exchange coupling strength (in J/m^2), $\mathbf{M}_n^\pm$ are the magnetization vectors evaluated on $\partial\Omega_n^\pm$, and $\mathbf{M}_n^\infty = \mathbf{M}_n(\infty)$, with the last term introduced to avoid divergent integrals. A non-dimensionalization as in (4), followed by the asymptotic expansion in $\delta \ll 1$ then results in $\mathcal{E}_J(\mathbf{M})/(Ad) \simeq E_N^\lambda(\mathbf{m}_1, \dots, \mathbf{m}_N)$, where

$$\begin{aligned}E_N^\lambda(\mathbf{m}_1, \dots, \mathbf{m}_N) &= E_N(\mathbf{m}_1, \dots, \mathbf{m}_N) \\ &\quad + \frac{\lambda}{2}\sum_{n=1}^{N-1}\int_{\mathbb{R}^2}\Big(|\mathbf{m}_n - \mathbf{m}_{n+1}|^2 - |\mathbf{m}_n^\infty - \mathbf{m}_{n+1}^\infty|^2\Big)d^2r,\end{aligned} \tag{36}$$

with $\lambda = J/(dK_d)$ the dimensionless interlayer coupling strength and $\mathbf{m}_n^\infty = \mathbf{m}_n(\infty)$. It is easy to see that if the interlayer exchange coupling strength is similar to the intralayer exchange, we have $\lambda \sim 1/\delta^2 \gg 1$.

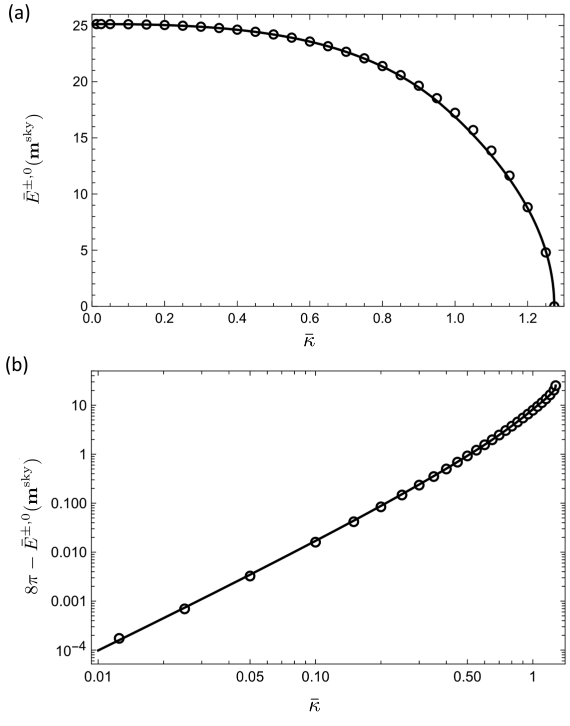

FIG. 4. Comparison of the skyrmion energy obtained numerically (open circles) with the prediction of (37) (solid lines): (a) the graph of $\bar{E}^{\pm,0}(\mathbf{m}^{\rm sky})$ vs. $\bar{\kappa}$; (b) the graph of $8\pi - \bar{E}^{\pm,0}(\mathbf{m}^{\rm sky})$ vs. $\bar{\kappa}$.

For SAF in the form of a bilayer, we have $N = 2$, $\lambda < 0$ and $|\lambda| \gg 1$, which forces antiferromagnetic order: $\mathbf{m}_1 \simeq \mathbf{m}$ and $\mathbf{m}_2 \simeq -\mathbf{m}$ for some $\mathbf{m} : \mathbb{R}^2 \to \mathbb{S}^2$. As a result, to the leading order in $|\lambda| \gg 1$ we have, after a further rescaling of space, $\bar{E}_2^\lambda \simeq 2\bar{E}^{\pm,0}$, where $\bar{E}^{\pm,0}$ is given by (14) with $\bar{\delta} = 0$. It corresponds to the classical two-dimensional micromagnetic energy without non-local effects that has been extensively studied [54, 57–59, 68–73]. The asymptotic behavior of the skyrmion energy as $\bar{\kappa} \to 0$ was established in [54] (see also [55, 70, 71]), while the asymptotic behavior for $\bar{\kappa} \to \bar{\kappa}_c = 4/\pi$ was established in [57] (see also [58]). Various ad-hoc formulas for the skyrmion energy have been proposed [59, 72, 73]. These are able to produce reasonable approximations for the skyrmion energy for certain ranges of $\bar{\kappa}$, but fail to provide a uniformly accurate approximation for the entire expected range $0 < \bar{\kappa} < \bar{\kappa}_c$ of skyrmion existence. Here we rectify this issue by providing a formula for the skyrmion collapse energy barrier $\Delta\bar{E}_2^{c,0} = 16\pi - 2\bar{E}^{\pm,0}(\mathbf{m}^{\rm sky})$ that agrees within a relative error of 6% for the entire range of $\bar{\kappa}$ with the one calculated from the "exact" skyrmion energy obtained from the numerical solution of the Euler-Lagrange equation associated with $\bar{E}^{\pm,0}(\mathbf{m}^{\rm sky})$ by the shooting method. The formula reads

$$\bar{E}^{\pm,0}(\mathbf{m}^{\rm sky}) \simeq \begin{cases} 8\pi - \frac{2\pi\bar{\kappa}^2}{\ln\left[\frac{\alpha}{\bar{\kappa}}\ln\left(\frac{16\alpha}{\bar{\kappa}}\right)\right]} & 0 < \bar{\kappa} \le 1, \\ 8\pi\beta\sqrt{2(\bar{\kappa}_c - \bar{\kappa})/\bar{\kappa}_c} & 1 < \bar{\kappa} < \bar{\kappa}_c, \end{cases} \tag{37}$$

where $\alpha = 4e^{-1-\gamma} \approx 0.8262$ and $\beta = 1.025$. The small $\bar{\kappa}$ formula is obtained from the result in [54] by keeping the $O(\ln|\ln\bar{\kappa}|/|\ln\bar{\kappa}|)$ term in the expansion and fitting the constant in the inner logarithm to the numerical data, while the large $\bar{\kappa}$ formula is obtained from the expansions in [57, 58], with the coefficient of the square root slightly adjusted to fit the numerics. A comparison of the skyrmion energy predicted by (37) and the one obtained numerically is presented in Fig. 4. The formula also gives the skyrmion energy $\bar{E}^{\pm,0}(\mathbf{m}^{\rm sky})$ with a uniform relative error of at most 3% for all values of $\bar{\kappa}$.

We also mention an empirical formula obtained for the skyrmion radius $\bar{\rho}_{2,0}^{\rm sky}$ in the units of L_B for synthetic antiferromagnetic bilayers obtained in [22]:

$$\bar{\rho}_{2,0}^{\mathrm{sky}} = \frac{a\bar{\kappa}^2}{\bar{\kappa}_c\sqrt{\bar{\kappa}_c^2 - \bar{\kappa}^2}}, \tag{38}$$

where $a = 1.35$, which gives an approximation for $\bar{\rho}_{2,0}^{\mathrm{sky}}$ to within a 5% relative error in the range $0.35 \leq \bar{\kappa} \leq 1.15$, and within a 25% relative error in the range $0.2 \leq \bar{\kappa} \leq 1.2$. Notice that this formula fails to reproduce the asymptotic behavior of $\bar{\rho}_{2,0}^{\mathrm{sky}}$ as a function of $\bar{\kappa}$ for $\bar{\kappa} \to 0$ or $\bar{\kappa} \to \bar{\kappa}_c$ [54, 57, 70].

To summarize, in a SAF, the skyrmion solutions have their energies and radii independent of $\bar{\delta}$ due to the cancellation of the non-local magnetostatic interactions. Another consequence of the vanishing stray field is the absence of bursting and the persistence of the skyrmion solution up to $\bar{\kappa}_c$. However, as can be seen from Fig. 4(b), the skyrmion collapse energy is dropping quickly away from $\bar{\kappa}_c$.

B. Ferromagnetic monolayers

We finally discuss the case of ferromagnetic monolayers, which also applies to symmetric ferromagnetic multilayers with strong ferromagnetic exchange coupling, $\lambda \gg 1$ in (36), upon taking d to be the sum of all the ferromagnetic layer thicknesses. We start by noting that for ultrathin monolayers, the skyrmion solutions in the low $\bar{\kappa}$ and $\bar{\delta}$ regime were characterized in our previous work by rigorous asymptotic analysis [44, 54, 55]. Skyrmions exhibit compact profiles close to the Belavin-Polyakov profiles and a reorientation from the Néel rotation at $\bar{\delta} = 0$ to the Bloch rotation at $\bar{\kappa} = 0$. For larger $\bar{\kappa}$ and $\bar{\delta}$, beyond the compact skyrmion limit, Büttner et al. [10] calculated numerically the skyrmion characteristics using a 360°-wall ansatz, without computing the skyrmion bursting threshold. This threshold was discussed by Bernand-Mantel et al. [11] and characterized by a numerical study of an analytical model based on the thin wall approximation valid for layer thicknesses much larger than the Bloch wall width, $d \gg L_B$ [74]. The model and the numerical solutions presented here complement those previous findings in the ultrathin film regime, $d \lesssim L_B$, and not too small DMI strengths, which forces the Néel rotation. As the analysis follows closely the steps of Sec. III, we only provide the necessary modifications and then present the numerical results obtained for the monolayer.

As was shown in [54], skyrmion solutions exist for all $0 < 2\bar{\kappa} + \bar{\delta} \leq \sqrt{2}$, with the profiles of Néel type for all $\bar{\delta} \leq \frac{32}{3\pi^2}\bar{\kappa}$ and all sufficiently small $\bar{\kappa}$. For larger values of $\bar{\kappa}$, one can carry out the same analysis as in Sec. III D to obtain the following expression for the energy of a bubble-like profile in (19):

$$\bar{E}_1(\mathbf{m}_{\bar{\rho}}) \simeq 2\pi\bar{\rho}\left[4 - \pi\bar{\kappa} + \frac{2\bar{\delta}\ln 2}{\pi}\right] + \frac{4\pi}{\bar{\rho}} - 4\bar{\delta}\bar{\rho}\ln\left(\frac{8\bar{\rho}}{\pi}e^{\gamma-1}\right), \tag{39}$$

to the leading order in $\bar{\rho} \gg 1$, where we accounted for an additional energy penalty arising from the volume-volume charge interactions [75, 76]. Here the profile is expected to retain its Néel character in a much broader range $\bar{\delta} \leq \frac{\pi^2}{4\ln 2}\bar{\kappa}$ corresponding to the threshold for a 1D domain wall [76].

As in the case of antisymmetric bilayers, the expression in (39) predicts the existence of a critical value of $\bar{\kappa} = \bar{\kappa}_1^b$ given by

$$\bar{\kappa}_1^b \simeq \frac{4}{\pi} - \frac{\bar{\delta}}{\pi^2}\left[\ln\left(\frac{32}{\pi\bar{\delta}}\right) + 2\gamma + 1\right], \tag{40}$$

such that two critical points of $\bar{E}_1(\mathbf{m}_{\bar{\rho}})$ exist for all $\bar{\kappa} < \bar{\kappa}_1^b(\bar{\delta})$, while the energy is monotonically decreasing for all $\bar{\kappa} > \bar{\kappa}_1^b(\bar{\delta})$, indicating skyrmion bursting at $\bar{\kappa} = \bar{\kappa}_1^b$. The formula is expected to be valid for $\bar{\delta} \lesssim 1$.

The expression in (39) may also be used to predict the energy barrier against bursting. When $\bar{\kappa}$ is not too close to $\bar{\kappa}_c$, the saddle point radius $\bar{\rho}_1^{\mathrm{sad}}$ may be obtained by dropping the $4\pi/\bar{\rho}$ term from (39) and finding the critical point of the energy

$$\bar{\rho}_1^{\mathrm{sad}} \simeq \frac{\pi}{4}\exp\left(\frac{2\pi}{\bar{\delta}} - \frac{\pi^2\bar{\kappa}}{2\bar{\delta}} - \gamma\right). \tag{41}$$

The associated bursting energy barrier is $\Delta\bar{E}_1^b = \bar{E}_1(\mathbf{m}_{\bar{\rho}_1^{\mathrm{sad}}}) - \bar{E}_1(\mathbf{m}^{\mathrm{sky}})$, where

$$\bar{E}_1(\mathbf{m}_{\bar{\rho}_1^{\mathrm{sad}}}) \simeq \pi\bar{\delta}\exp\left(\frac{2\pi}{\bar{\delta}} - \frac{\pi^2\bar{\kappa}}{2\bar{\delta}} - \gamma\right), \tag{42}$$

and $\bar{E}_1(\mathbf{m}^{\mathrm{sky}})$ is the energy of the skyrmion solution. The collapse barrier, on the other hand, is $\Delta\bar{E}_1^c = 8\pi - \bar{E}_1(\mathbf{m}^{\mathrm{sky}})$ [10, 11, 54, 59, 61], so equating the two we obtain the predicted optimal value $\bar{\kappa}_1^{\mathrm{opt}}$ at which the skyrmion lifetime is maximized at fixed $\bar{\delta} \lesssim 1$:

$$\bar{\kappa}_1^{\mathrm{opt}} \simeq \frac{4}{\pi} - \frac{2\bar{\delta}}{\pi^2}\ln\left(\frac{8e^{\gamma}}{\bar{\delta}}\right). \tag{43}$$

We finally note that the relation in (33) also holds in the case of monolayers for $\bar{\delta} \ll 1$ and $\bar{\kappa}$ not too close to $\bar{\kappa}_c$ (cf. [62]).

We conclude this section by carrying out the simulations for monolayers that are analogous to those of Sec. III G. All the simulations use the same parameters as in Sec. III G, except the computational grid used is $2048 \times 2048 \times 1$. The computed dimensionless skyrmion radius $\bar{\rho}_1^{\mathrm{sky}}$ and energy $\bar{E}_1(\mathbf{m}^{\mathrm{sky}})$ as functions of $\bar{\kappa}$ and $\bar{\delta}$ are presented in Figs. 5(a) and 5(b). In turn,

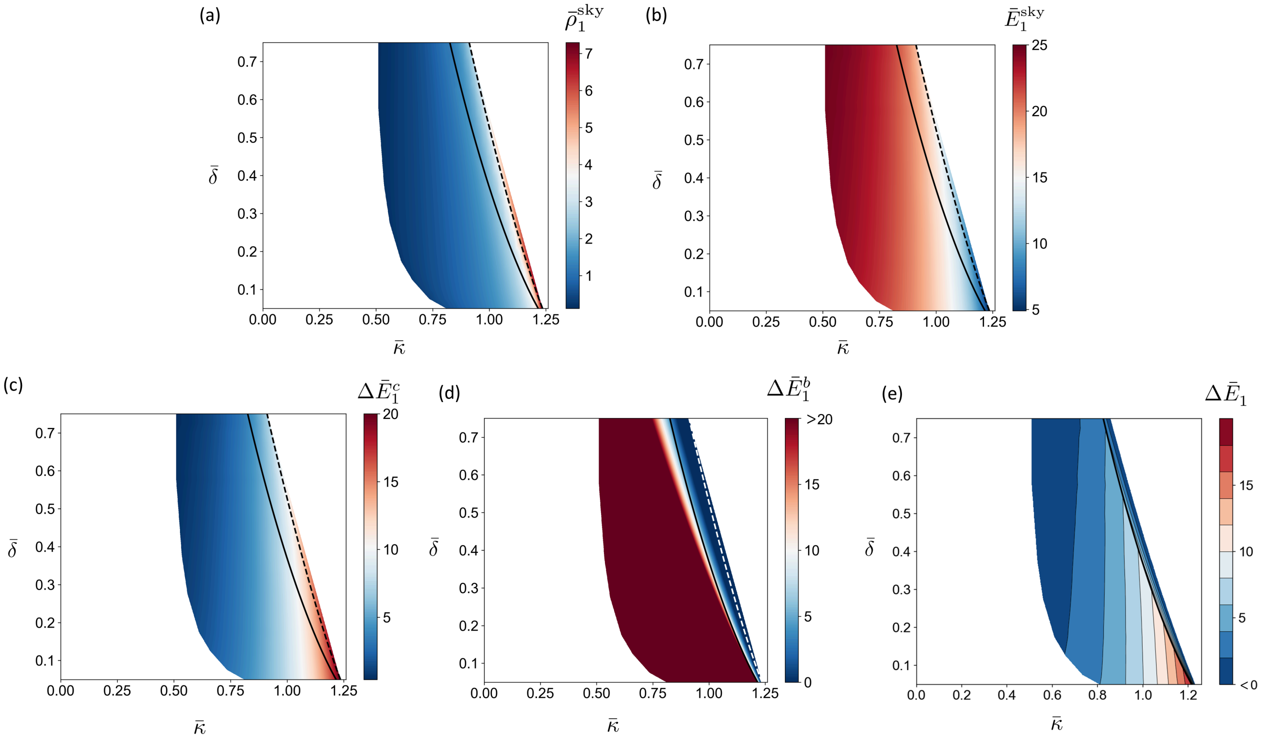

FIG. 5. Summary of the numerical results obtained from MUMAX3 simulations (see Sec. IV B for details) of a ferromagnetic monolayer with the same parameters as in Fig. 3: (a) the dimensionless radius $\bar{\rho}_1^{\mathrm{sky}}$; (b) the dimensionless skyrmion energy $\bar{E}_1^{\mathrm{sky}}$; (c) the dimensionless collapse energy barrier $\Delta\bar{E}_1^c$; (d) the dimensionless bursting energy barrier $\Delta\bar{E}_1^b$; (e) the dimensionless effective energy barrier $\Delta\bar{E}_1$. The solid line shows $\bar{\kappa}_1^{\mathrm{opt}}(\bar{\delta})$, while the dashed line shows $\bar{\kappa}_1^b(\bar{\delta})$, governed, respectively, by (43) and (40).

the dimensionless collapse energy barrier $\Delta\bar{E}_1^c = 8\pi - \bar{E}_1(\mathbf{m}^{\mathrm{sky}})$ is plotted in Fig. 5(c), while the bursting energy barrier $\Delta\bar{E}_1^b = \bar{E}_1(\mathbf{m}^{\mathrm{sad}}) - \bar{E}_1(\mathbf{m}^{\mathrm{sky}})$, where $\bar{E}_1(\mathbf{m}^{\mathrm{sad}}) \simeq \bar{E}_1(\mathbf{m}_{\bar{\rho}_1^{\mathrm{sad}}})$ is given by (42) is plotted in Fig. 5(d). The effective energy barrier $\Delta\bar{E}_1 = \min(\Delta\bar{E}_1^c, \Delta\bar{E}_1^b)$ is shown in Fig. 5(e).

Contrary to the case of antisymmetric bilayers, the skyrmion solution radii and collapse barriers in Figs. 5(a) and 5(c) show mostly an increase with increasing $\bar{\kappa}$, while their variation with $\bar{\delta}$ is weak. Again, the absence of the numerical skyrmion solution for low $\bar{\kappa}$ and $\bar{\delta}$ is due to the fixed finite discretization in the film plane that is unable to resolve the skyrmion of vanishingly low radius and leads to a numerical collapse (see also the discussion in Section III G). As in the case of the antisymmetric bilayer in Sec. III G, for large values of $\bar{\kappa}$ and $\bar{\delta}$ we observe bursting of the skyrmion, which shows a very good agreement with the predicted bursting threshold $\bar{\kappa}_1^b(\bar{\delta})$ from (40), represented by a dashed line in Fig. 5. Below the optimal stability threshold $\bar{\kappa}_1^{\mathrm{opt}}(\bar{\delta})$ (solid line), the effective energy barrier shown in Fig. 5(e), shows a weak dependence on $\bar{\delta}$. In fact, we observe that, contrary to the antisymmetric bilayer case, the level lines of sufficiently high effective energy barrier are covering very narrow ranges of $\bar{\kappa}$ values.

C. Comparison of skyrmion solutions for a typical ferromagnetic material

We now demonstrate how the obtained results can be used to predict skyrmion stability against thermal noise, using a typical family of ferromagnetic materials, the Pt/Co/AlO$_x$ system, as a building block to construct the three types of stacking in Fig. 1.

We begin by pointing out the fundamental energy scale associated with the thermally activated processes in ultra-thin film micromagnetics, namely, the energy of a "zero-radius skyrmion" in a monolayer, $\Delta\mathcal{E}_0 = 8\pi Ad$, corresponding to the energy of the minimizers of the exchange energy alone in the form of Belavin-Polyakov profiles [77]. With the parameters that we chose to represent a characteristic ferromagnetic Pt/Co/AlO$_x$ layer in Sec. III G, $A = 20$ pJ/m and d=1 nm, we have $\Delta\mathcal{E}_0 \approx 120 k_B T_{RT}$, where $T_{RT} = 300K$ is the room temperature. It sets an upper bound for the collapse energy barrier.

As this fundamental energy scale $\Delta\mathcal{E}_0$ increases with the film thickness, it is natural to consider stacking multiple ferromagnetic layers to enhance the effective thickness without decreasing the DMI [10]. However, as we show in the present work, when d is increased, the stray field effects get stronger and the skyrmion solution disappears above a critical value of the thickness corresponding to the bursting threshold determined by (21) or (40) in the cases of antisymmetric bilayers or monolayers, respectively. An additional difficulty is the dependence of the micromagnetic parameters on the film thickness [63, 66], so predictions about skyrmion existence and stability require the knowledge of all these specific dependences.

To circumvent this difficulty, in the following we make a simplifying assumption that the ferromagnet exhibits a bulk perpendicular magnetocrystalline anisotropy $K_u > K_d$ independent of d and a negligible interfacial anisotropy $K_s = 0$ (in J/m^2). While in principle the magnetocrystalline anisotropy is of interfacial origin in the Pt/Co/AlO$_x$ system, this choice enables us to highlight the effect of the modulation of the stray field via the dimensional thickness change independently of the anisotropy change. This is also experimentally justified, considering the recent finding in Pt/Co/AlO$_x$ of a strong anisotropy tuning, at fixed Co thickness, via a thickness increase of the capping Al layer, which enables an independent tuning of Co thickness and anisotropy in this system [66]. We also assume that the DMI is of interfacial origin, which corresponds to a DMI constant per unit volume $D = D_s/d$ (in the units of J/m^2) with the interfacial DMI strength D_s (in the units of J/m) independent of d.

With the above assumptions, we study the resulting dependence of the energy barriers governing skyrmion stability on the parameters and, in particular, on the film thickness as the most easily adjustable material parameter. It is clear that since the barrier height vanishes as $d \to 0$ due to the dimensional Ad factor, and since the solution disappears for d above a critical value depending on the rest of the parameters, there must exist a set of parameters for which the energy barrier attains its maximum value.

The predicted dependences of the skyrmion radius R and the effective energy barrier $\Delta\mathcal{E}$ on D_s and d for an antisymmetric bilayer, a SAF and a ferromagnetic monolayer with $A = 20$ pJ/m, $M_s = 1$ MA/m and $K_u = 0.9$ MJ/m^3, in the physically realizable range $0 < D_s < D_s^{\max}$ with $D_s^{\max} \simeq 2$ pJ/m [63, 66], are presented in Fig. 6. These graphs are obtained by replotting the dimensional skyrmion radii R and the effective energy barriers $\Delta\mathcal{E}$ calculated from the dimensionless radii $\bar\rho$ and effective energy barriers $\Delta\bar E$ obtained in the previous sections as functions of $\bar\kappa$ and $\bar\delta$ expressed in terms of the interfacial DMI strength D_s and the single ferromagnetic layer thickness d. As our aim is to focus on room temperature stability, we only present the skyrmion solutions with effective barriers $\Delta\mathcal{E} > 20 k_B T_{RT}$ in Fig. 6.

For antisymmetric bilayers in Figs. 6(a) and 6(d), we present the radii R and the effective energy barriers $\Delta\mathcal{E}$ of skyrmions as functions of D_s and d (see figure caption for details). The skyrmion solutions are extending across a large crescent-shaped region. The maximum effective energy barrier in the crescent is reaching $\simeq 62 k_B T_{RT}$ at $D_s \simeq 1.74$ pJ/m and $d \simeq 1.4$ nm, and corresponds to a skyrmion solution of radius $R \simeq 11$ nm. We note that the optimal skyrmion stability occurs, for every thickness d, in the close vicinity of $D_s = D_{s,\mathrm{opt}}^{\mathrm{bi}}$, represented by a dashed line in Figs. 6(a) and 6(d), that is obtained from (28):

$$D_{s,\mathrm{opt}}^{\mathrm{bi}} \simeq \frac{4d}{\pi}\sqrt{A(K_u - K_d)} - \frac{4d^2 K_d}{\pi^2}\left[\ln\left(\frac{8\sqrt{A(K_u-K_d)}}{dK_d}\right) + \gamma + \frac{\pi^2}{8}\right]. \quad (44)$$

The barrier height remains uniformly higher than $50 k_B T_{RT}$ in a broad range of thicknesses and in a certain range of D_s, with the radii varying from 8 nm to 15 nm. For example, the cross-section of the plot in Fig. 6(d) at $D_s = 1.7$ pJ/m is shown in Fig. 7, indicating this large range of thermal stability against variatons of d. These results identify the antisymmetric bilayer as a promising platform for 10 nm radius zero-field skyrmions with lifetimes compatible with information technology applications.

For SAF in the form of a bilayer, in Figs. 6(b) and 6(e) we display the radii R and the collapse energy barriers $\Delta\mathcal{E}$ as functions of D_s and d (see figure caption for details). Here the region of relative stability ($\Delta\mathcal{E} \geq 20 k_B T_{RT}$) has the form of a wedge, in which the barrier height can reach its theoretical maximum of $16\pi Ad$ as $D = D_s d$ approaches $D_c = \frac{4}{\pi}\sqrt{A(K_u - K_d)}$. For the same value of $D_s = 1.74$ pJ/m that optimizes skyrmion stability in antisymmetric bilayers, we have $D_c \simeq 3$ mJ/m^2 and $\Delta\mathcal{E} \simeq 145 k_B T_{RT}$ at a critical thickness d_c finely tuned to around 0.6 nm. The region where the barrier height remains higher than $50 k_B T_{RT}$ extends over a fairly broad region of D_s values larger than 0.8 pJ/m and thicknesses below $d = 1$ nm. The skyrmion solution radii are increasing as one gets closer to the critical DMI line $D = D_c$. Note that due to the absence of a saddle point, the expected skyrmion behavior close to the critical DMI value D_c will be very different from that of a skyrmion in an antisymmetric bilayer or a monolayer close to the bursting line. In particular additional entropic contributions to the collapse energy barrier [78, 79] would become increasingly important as D approaches D_c due to the vanishing domain wall stiffness as $D \to D_c$; such a study would go beyond the scope of the present paper.

Finally, Figs. 6(c) and 6(f) show the radii R and effective energy barriers $\Delta\mathcal{E}$ of skyrmions as a function of D_s and d for a ferromagnetic monolayer (see figure caption for details). The region of relative stability ($\Delta\mathcal{E} \geq 20 k_B T_{RT}$) extends over a much narrower wedge-shaped zone as compared to the asymmetric bilayer and SAF. The effective energy barrier reaches up to about $45 k_B T_{RT}$. This, however, requires a very sharp tuning of the layer thickness d around 0.7 nm and D_s around 2 pJ/m or beyond.

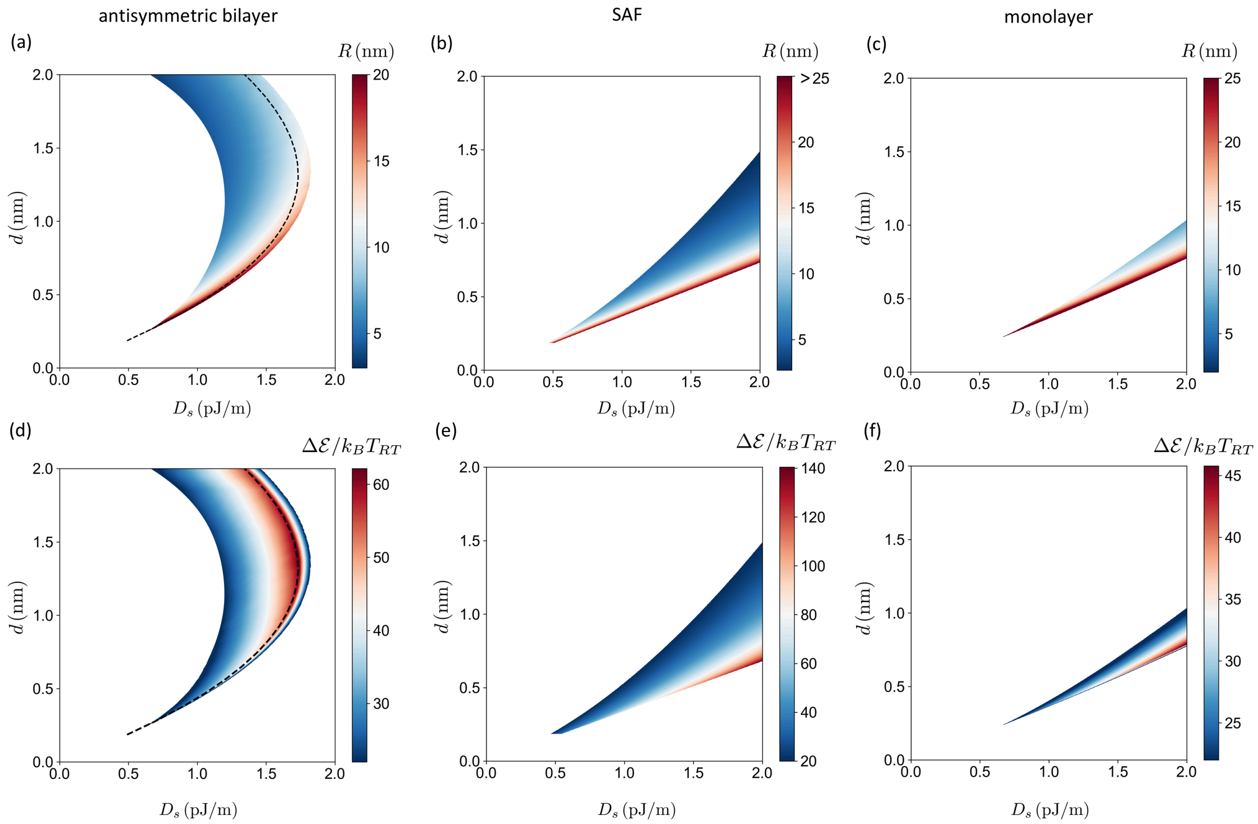

FIG. 6. Skyrmion radius R (a)-(c) and effective energy barrier $\Delta\mathcal{E}$ in the units of k_BT_{RT} (d)-(f), where we excluded skyrmion solutions with $\Delta\mathcal{E} < 20k_BT_{RT}$, as functions of the interfacial DMI strength D_s and the single ferromagnetic layer thickness d for: (a,d) antisymmetric ferromagnetic bilayer; (b,e) SAF ; (c,f) ferromagnetic monolayer. In (a) and (d): dimensional versions of the skyrmion radius $R = \bar{\rho}_2^{\text{sky}} L_B$ and the effective energy barrier $\Delta\mathcal{E} = Ad\Delta\bar{E}_2$ are dimensional replots of the data from the skyrmion solutions presented in Figs. 3(a) and 3(e) from Sec. III G. In (b) and (e): dimensional versions of the skyrmion radius $R = \bar{\rho}_{2,0}^{\text{sky}} L_B$, where $\bar{\rho}_{2,0}^{\text{sky}}$ is given by (38), and effective energy barrier $\Delta\mathcal{E} = Ad\Delta\bar{E}_2^{c,0}$ where $\Delta\bar{E}_2^{c,0}$ is given by (37). In (c) and (f): the dimensional version of the skyrmion radius $R = \bar{\rho}_1^{\text{sky}} L_B$ and the barrier $\Delta\mathcal{E} = Ad\Delta\bar{E}_1$ are dimensional replots of the data from the skyrmion solutions presented in Figs. 5(a) and 5(e) from Sec. IV B. Other parameters in this figure are: $A = 20$ pJ/m, $M_s = 1$ MA/m, $K_u = 0.9$ MJ/m^3 and $K_s = 0$ J/m^2. The dashed line in (a) and (d) shows $D_{s,\text{opt}}^{\text{bi}}$ vs. d from (44).

V. CONCLUSIONS

Since the first observations of skyrmions and their displacement with low electric current densities, considerable efforts have been devoted to the practical realization of order 10 nm radius skyrmions existing at zero applied magnetic field with the liftime and dynamics compatible with information technology applications. In this quest, for a long time the stray field effects have been generally ignored, considered negligible because of the ultrathin characteristics of the magnetic layers in which the skyrmions appeared and/or because of the presence of strong, dominating DMI. In later developments, stray field effects have been seen as a source of instability, as they promote the enlargement of skyrmions and their disappearance via bursting or stripe-out, as observed in many experiments on ferromagnetic mono- and multilayers.

In the present study, we demonstrated that, to the contrary, the stray field may exert a pronounced stabilizing effect on magnetic skyrmions. We established that in exchange-decoupled antisymmetric bilayers the stray field and the DMI are tailored to be highly favorable to skyrmion stability through a coordinated action of the DMI and the dipolar interaction to form a chiral pair of skyrmions in a flux-closure pattern.

To fully assess the performance of this system, we carried out a combined analytical and computational micromagnetic study, focusing on the parameter regime in which the skyrmions have the form of tiny magnetic bubbles whose shape may be characterized by a single parameter — the skyrmion radius. In particular, we obtained an accurate representation of the stray field energy of a skyrmionic bubble as a function of its radius

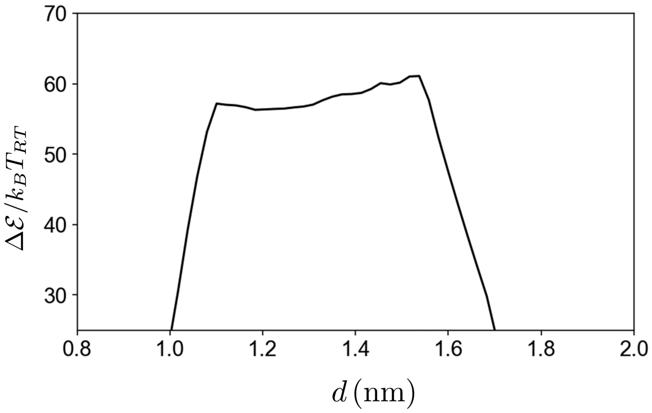

FIG. 7. Effective energy barrier $\Delta\mathcal{E}$ in the units of $k_B T_{RT}$ as a function of d obtained from Fig. 6(e) for the antisymmetric ferromagnetic bilayer with fixed $D_s = 1.7$ pJ/m.

that is asymptotically valid for sufficiently thin films and the radii exceeding the transition layer thickness of the skyrmionic bubble. In this regime, we obtained zero magnetic field skyrmion phase diagrams as a function of only two dimensionless parameters, the reduced DMI strength and the reduced film thickness, governing the system's behavior.

The importance of the obtained phase diagrams lies in the fact that they provide, for the first time, the region of skyrmion stability via a quantitative prediction of skyrmion bursting, in agreement with the numerics. They also give a prediction for the effective energy barrier that determines skyrmion stability against thermal noise and allows to locate the material parameters for which this stability is optimal. We wish to point out the very important role of the analytical modeling in our work for guiding the micromagnetic simulations: it is the knowlege of the position of the optimal skyrmion stability line and the use of the skyrmion solution configurations along it as starting points for the simulations that enabled us to obtain a full phase diagrams in the non-dimensional parameter space within a practical computational time.

The non-dimensional phase diagrams can, in turn, be used to predict the skyrmion size and stability across a broad spectrum of micromagnetic parameters, as demonstrated in the case of Pt/Co/AlO$_x$ based materials. Using this example, we illustrated the potential of the exchange-decoupled antisymmetric ferromagnetic layers and compared it with that of SAF and ferromagnetic monolayers. We found that the antisymmetric bilayer provides a broadening of the range of existence of skyrmion solutions, which could potentially result in a significant decrease of the degree of fine-tuning necessary to obtain very compact and stable skyrmions. We hope that our findings, together with the recent experimental verification of a dipolar-field-enhanced effective DMI in antisymmetric bilayers, will motivate further experimental studies into stray-fields-assisted skyrmion stabilization.

ACKNOWLEDGMENTS

A. Bernand-Mantel was supported by France 2030 government investment plan managed by the French National Research Agency under grant reference PEPR SPIN ANR-22-EXSP-0009 and grant NanoX ANR-17-EURE-0009 in the framework of the Programme des Investissements d'Avenir. C. B. Muratov was supported by MUR via PRIN 2022 PNRR project P2022WJW9H and acknowledges the MUR Excellence Department Project awarded to the Department of Mathematics, University of Pisa, CUP I57G22000700001. C. B. Muratov is a member of INdAM-GNAMPA. The authors would also like to express their gratitude for the hospitality of the Isaac Newton Institute within the scope of the program "Recent challenges in the mathematical design of new materials", during which some of the ideas of this work had been conceived.

Appendix A: Computation of the stray field energy

In this section we compute the non-local surface-surface charge contribution to the magnetostatic energy for the configuration in (19), which is defined by

$$E_{ss}(m^{\parallel}) = -\bar{\delta} \int_{\mathbb{R}^2} \int_{\mathbb{R}^2} \frac{\nabla m^{\parallel}(\mathbf{r}) \cdot \nabla m^{\parallel}(\mathbf{r}')}{4\pi|\mathbf{r}-\mathbf{r}'|} \, d^2r \, d^2r'. \tag{A1}$$

We introduce the 2D Fourier transform

$$\widehat{f}(\mathbf{q}) = \int_{\mathbb{R}^2} e^{-i\mathbf{q}\cdot\mathbf{r}} f(\mathbf{r}) \, d^2r, \tag{A2}$$

and note that

$$\begin{aligned} E_{ss}(m^{\parallel}) &= -\frac{\bar{\delta}}{2} \int_{\mathbb{R}^2} q \, |\widehat{m^{\parallel}+1}|^2 \frac{d^2q}{(2\pi)^2} \\ &= -\frac{\bar{\delta}}{2} \|m^{\parallel}+1\|^2_{\mathring{H}^{1/2}(\mathbb{R}^2)}, \end{aligned} \tag{A3}$$

where $q = |\mathbf{q}|$ and $\|m^{\parallel}+1\|^2_{\mathring{H}^{1/2}(\mathbb{R}^2)}$ is the homogenous Gagliardo norm squared of $m^{\parallel}+1$, that may be alternatively defined as [80, 81]

$$\|m^{\parallel}+1\|^2_{\mathring{H}^{1/2}(\mathbb{R}^2)} = \int_{\mathbb{R}^2} \int_{\mathbb{R}^2} \frac{(m^{\parallel}(\mathbf{r}) - m^{\parallel}(\mathbf{r}'))^2}{4\pi|\mathbf{r}-\mathbf{r}'|^3} d^2r \, d^2r'. \tag{A4}$$

We wish to compute the norm in the expression for

$E_{ss}(m^{\|})$ asymptotically for $\bar{\rho} \gg 1$. To this aim, we define

$$\begin{aligned}\widehat{m^{\|}+1} &= \int_{\mathbb{R}^2} e^{-i\mathbf{q}\cdot\mathbf{r}}(m^{\|}+1)\,d^2r \\ &= \int_0^{2\pi}\int_0^{\infty} e^{-iqr\cos\theta}(1+\tanh(\bar{\rho}-r))r\,dr\,d\theta \\ &= 2\pi I, \end{aligned} \tag{A5}$$

where

$$I = \int_0^{\infty} J_0(qr)[1+\tanh(\bar{\rho}-r)]r\,dr, \tag{A6}$$

and here and below $J_n(z)$ is the Bessel function of the first kind of order n [82]. Note that $1+\tanh(\bar{\rho}-r)$ decays exponentially to 0 as $r\to\infty$, and hence the above integral converges absolutely for all q and $\bar{\rho}$.

We introduce a new variable $y = r/\bar{\rho}$ and perform an integration by parts:

$$\begin{aligned} I &= \bar{\rho}^2\int_0^{\infty} yJ_0(q\bar{\rho}y)[1+\tanh(\bar{\rho}(1-y))]\,dy \\ &= \frac{\bar{\rho}^2}{q}\int_0^{\infty} yJ_1(q\bar{\rho}y)\,\mathrm{sech}^2(\bar{\rho}(1-y))\,dy, \end{aligned} \tag{A7}$$

where we used the identity $[zJ_1(z)]' = zJ_0(z)$ [82]. We then again change variables to $z = \bar{\rho}(1-y)$ and obtain $I = \bar{\rho}I_0/q$, where

$$I_0 = \int_{-\infty}^{\bar{\rho}}\left(1-\frac{z}{\bar{\rho}}\right)J_1(q\bar{\rho}-qz)\,\mathrm{sech}^2 z\,dz. \tag{A8}$$

For each q fixed and $\bar{\rho}\gg 1$ the integrand in (A8) is exponentially small for all $z > \bar{\rho}$. Therefore, we can extend the domain of integration in (A8) to the whole of $\mathbb{R}$ to obtain that to within $O(e^{-\bar{\rho}})$

$$I_0 \simeq \int_{-\infty}^{\infty}\left(1-\frac{z}{\bar{\rho}}\right)J_1(q\bar{\rho}-qz)\,\mathrm{sech}^2 z\,dz. \tag{A9}$$

Now we utilize the integral representation of the Bessel function [82]

$$J_1(z) = \frac{1}{\pi}\int_0^{\pi}\sin\theta\sin(z\sin\theta)\,d\theta, \tag{A10}$$

and change the order of integration, arriving at

$$\begin{aligned} I_0 \simeq \frac{1}{\pi}\int_0^{\pi}\sin\theta\Bigg\{\int_{-\infty}^{\infty}\left(1-\frac{z}{\bar{\rho}}\right)\mathrm{sech}^2 z \\ \times\sin\left[(q\bar{\rho}-qz)\sin\theta\right]\,dz\Bigg\}\,d\theta. \end{aligned} \tag{A11}$$

Using basic trigonometry, we can write

$$\begin{aligned} &\int_{-\infty}^{\infty}\left(1-\frac{z}{\bar{\rho}}\right)\mathrm{sech}^2 z\sin[(q\bar{\rho}-qz)\sin\theta]\,dz = \\ &\quad\sin(q\bar{\rho}\sin\theta)\int_{-\infty}^{\infty}\left(1-\frac{z}{\bar{\rho}}\right)\mathrm{sech}^2 z\cos(qz\sin\theta)\,dz \\ &\quad-\cos(q\bar{\rho}\sin\theta)\int_{-\infty}^{\infty}\left(1-\frac{z}{\bar{\rho}}\right)\mathrm{sech}^2 z\sin(qz\sin\theta)\,dz. \end{aligned} \tag{A12}$$

Then, due to the even and odd symmetries of the functions involved in the integrands we can simplify this to

$$\begin{aligned} &\int_{-\infty}^{\infty}\left(1-\frac{z}{\bar{\rho}}\right)\mathrm{sech}^2 z\sin[(q\bar{\rho}-qz)\sin\theta]\,dz = \\ &\quad\sin(q\bar{\rho}\sin\theta)\int_{-\infty}^{\infty}\mathrm{sech}^2 z\cos(qz\sin\theta)\,dz \\ &\quad+\frac{1}{\bar{\rho}}\cos(q\bar{\rho}\sin\theta)\int_{-\infty}^{\infty}z\,\mathrm{sech}^2 z\sin(qz\sin\theta)\,dz. \end{aligned} \tag{A13}$$

The integrals appearing in the right-hand side of the above expression are evaluated as

$$\int_{-\infty}^{\infty}\mathrm{sech}^2 z\cos kz\,dz = \frac{\pi k}{\sinh(\pi k/2)}, \tag{A14}$$

$$\begin{aligned} &\int_{-\infty}^{\infty}z\,\mathrm{sech}^2 z\sin kz\,dz \\ &\qquad= \frac{\pi}{\sinh(\pi k/2)}\left[\frac{\pi k}{2}\coth\left(\frac{\pi k}{2}\right)-1\right]. \end{aligned} \tag{A15}$$

Setting $k = q\sin\theta$, we then have $I_0 \simeq I_1 + I_2$, where

$$I_1 = \int_0^{\pi}\frac{q\sin^2\theta\sin(q\bar{\rho}\sin\theta)}{\sinh(\frac{\pi q\sin\theta}{2})}\,d\theta, \tag{A16}$$

$$\begin{aligned} I_2 = \frac{1}{\bar{\rho}}\int_0^{\pi}&\frac{\sin\theta\cos(q\bar{\rho}\sin\theta)}{\sinh(\frac{\pi q\sin\theta}{2})} \\ &\times\left[\frac{\pi q\sin\theta}{2}\coth\left(\frac{\pi q\sin\theta}{2}\right)-1\right]\,d\theta. \end{aligned} \tag{A17}$$

Now, for each q fixed and $\bar{\rho}\gg 1$, we observe that I_1 and I_2 have highly oscillatory integrands and, therefore, we can use the stationary phase method (around $\theta = \frac{\pi}{2}$) [83, Proposition 3, Chapter 8] to evaluate the above integrals. After a few manipulations, we obtain to within $O(1/\bar{\rho})$ relative errors:

$$\begin{aligned} I_1 &\simeq q\,\mathrm{csch}\left(\frac{\pi q}{2}\right)\int_0^{\pi}\sin\theta\sin(q\bar{\rho}\sin\theta)\,d\theta \\ &= \pi q\,\mathrm{csch}\left(\frac{\pi q}{2}\right)J_1(q\bar{\rho}), \end{aligned} \tag{A18}$$

and

$$\begin{aligned} I_2 &\simeq \frac{1}{\bar{\rho}}\left[\frac{\frac{\pi q}{2}\coth\left(\frac{\pi q}{2}\right)-1}{\sinh\left(\frac{\pi q}{2}\right)}\right]\int_0^{\pi}\cos(q\bar{\rho}\sin\theta)\,d\theta \\ &= \frac{\pi J_0(q\bar{\rho})}{\bar{\rho}}\left[\frac{\frac{\pi q}{2}\coth\left(\frac{\pi q}{2}\right)-1}{\sinh\left(\frac{\pi q}{2}\right)}\right], \end{aligned} \tag{A19}$$

where we used (A10) and the integral representation [82]

$$J_0(z) = \frac{1}{\pi}\int_0^{\pi}\cos(z\sin\theta)\,d\theta. \tag{A20}$$

Notice that the above approximation for I_1 also remains valid for $q\bar{\rho}\lesssim 1$, as can be seen by Taylor-expanding the denominator of the integrand in $q\ll 1$ in this case.

We now observe that for $\bar\rho \gg 1$ the integral I_2 is negligible compared to I_1, and hence up to an $O(1/\bar\rho)$ relative error we have

$$I = \frac{\bar\rho I_0}{q} \simeq \frac{\bar\rho I_1}{q} \simeq \pi\bar\rho \operatorname{csch}\left(\frac{\pi q}{2}\right) J_1(q\bar\rho). \tag{A21}$$

It follows that

$$\widehat{m^\parallel + 1} = 2\pi I \simeq 2\pi^2 \bar\rho J_1(q\bar\rho) \operatorname{csch}\left(\frac{\pi q}{2}\right), \tag{A22}$$

and we have $\|m^\parallel + 1\|^2_{\mathring{H}^{1/2}(\mathbb{R}^2)} \simeq 2\pi^3\bar\rho^2 N$, where

$$N = \int_0^\infty q^2 J_1^2(q\bar\rho) \operatorname{csch}^2\left(\frac{\pi q}{2}\right) dq. \tag{A23}$$

We next choose $\sigma > 0$ such that $\sigma \ll 1$ and $\sigma\bar\rho \gg 1$, and split this integral as

$$\begin{aligned} N &= \int_0^\sigma q^2 J_1^2(q\bar\rho) \operatorname{csch}^2\left(\frac{\pi q}{2}\right) dq \\ &\quad + \int_\sigma^\infty q^2 J_1^2(q\bar\rho) \operatorname{csch}^2\left(\frac{\pi q}{2}\right) dq \\ &\simeq \frac{4}{\pi^2}\int_0^\sigma J_1^2(q\bar\rho)\, dq \\ &\quad + \frac{2}{\pi\bar\rho}\int_\sigma^\infty q \sin^2\left(q\bar\rho - \frac{\pi}{4}\right) \operatorname{csch}^2\left(\frac{\pi q}{2}\right) dq \\ &= N_1 + N_2, \end{aligned} \tag{A24}$$

to within an error bounded by a quantity of order $O(\sigma^3) + O(1/(\sigma\bar\rho^2))$, using the asymptotic formula [82]

$$J_1(z) \simeq \sqrt{\frac{2}{\pi z}} \sin\left(z - \frac{\pi}{4}\right), \qquad z \gg 1. \tag{A25}$$

For the second integral, we have for $\bar\rho \gg 1$

$$\begin{aligned} N_2 &= \frac{1}{\pi\bar\rho}\int_\sigma^\infty q\left[1 - \sin(2q\bar\rho)\right] \operatorname{csch}^2\left(\frac{\pi q}{2}\right) dq \\ &\simeq \frac{1}{\pi\bar\rho}\int_\sigma^\infty q \operatorname{csch}^2\left(\frac{\pi q}{2}\right) dq, \end{aligned} \tag{A26}$$

up to an error of order $O(1/(\sigma\bar\rho^2))$. Thus

$$N \simeq \frac{4}{\pi^2\bar\rho}\int_0^{\sigma\bar\rho} J_1^2(s)\, ds + \frac{1}{\pi\bar\rho}\int_\sigma^\infty q \operatorname{csch}^2\left(\frac{\pi q}{2}\right) dq. \tag{A27}$$

The second integral above is computable explicitly, and using $\sigma \ll 1$ we have asymptotically

$$\int_\sigma^\infty q \operatorname{csch}^2\left(\frac{\pi q}{2}\right) dq \simeq \frac{4}{\pi^2}\left(1 - \ln\pi - \ln\sigma\right), \tag{A28}$$

to within an $O(\sigma^2)$ error. The first integral is computable in terms of the generalized hypergeometric functions, and it is possible to find its asymptotic behavior to within an $O(1/(\sigma\bar\rho))$ error (arguing, e.g. as in [84]):

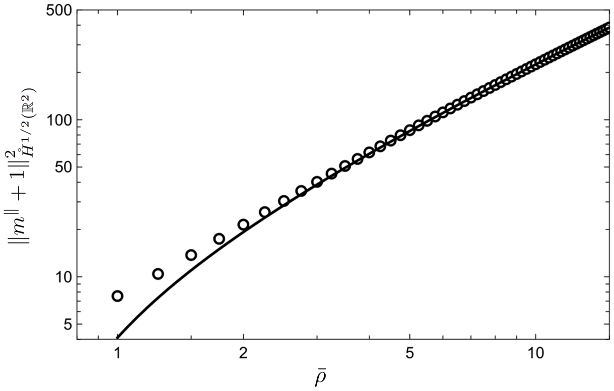

FIG. 8. Comparison of the quantity in the left-hand side of (A30) (open circles) with the prediction in the right-hand side (solid line).

$$\int_0^{\sigma\bar\rho} J_1^2(s)\, ds \simeq \frac{1}{\pi}\left(-2 + \gamma + 3\ln 2 + \ln\bar\rho + \ln\sigma\right). \tag{A29}$$

Using all these results, we finally obtain, up to a relative error of algebraic order in $1/\bar\rho$:

$$\|m^\parallel + 1\|^2_{\mathring{H}^{1/2}(\mathbb{R}^2)} \simeq 8\bar\rho \ln\left(\frac{8\bar\rho}{\pi} e^{\gamma - 1}\right), \tag{A30}$$

which is one of our principal results. To verify its accuracy, we evaluated the norm numerically for a range of $\bar\rho$, using the representation in (A4) and compared the result with the one given by (A30). Taking advantage of the radial symmetry, the computation of the norm may be reduced to the following double integral amenable to an accurate numerical evaluation [85, Eq. (3.617)]:

$$\begin{aligned} &\|m^\parallel + 1\|^2_{\mathring{H}^{1/2}(\mathbb{R}^2)} = \\ &\quad \int_0^\infty \int_r^\infty \left[\tanh(\bar\rho - r) - \tanh(\bar\rho - r')\right]^2 \\ &\quad \times \frac{4rr' \operatorname{E}\left(\frac{2\sqrt{rr'}}{r' + r}\right)}{(r' - r)^2 (r' + r)}\, dr'\, dr, \end{aligned} \tag{A31}$$

where $\operatorname{E}(k) = \int_0^{\pi/2} \sqrt{1 - k^2 \sin^2\theta}\, d\theta$ is the complete elliptic integral of the second kind. A comparison of the numerical results and the prediction of the formula in (A30) is presented in Fig. 8. One can see that already for $\bar\rho \geq 2$ the formula in the right-hand side of (A30) predicts the value of the norm to within $\sim 10\%$ accuracy, and the accuracy rapidly increases with $\bar\rho$.

---

[1] A. Fert, V. Cros, and J. Sampaio, Skyrmions on the track, Nature Nanotechnol. **8**, 152 (2013).

[2] A. Fert, N. Reyren, and V. Cros, Magnetic skyrmions: advances in physics and potential applications, Nat. Rev. Mater. **2**, 17031 (2017).

[3] X. Zhang, Y. Zhou, K. M. Song, T.-E. Park, J. Xia, M. Ezawa, X. Liu, W. Zhao, G. Zhao, and S. Woo, Skyrmion-electronics: writing, deleting, reading and processing magnetic skyrmions toward spintronic applications, J. Phys. – Condensed Matter **32**, 143001 (2020).

[4] O. Lee, R. Msiska, M. A. Brems, M. Kläui, H. Kurebayashi, and K. Everschor-Sitte, Perspective on unconventional computing using magnetic skyrmions, Appl. Phys. Lett. **122**, 260501 (2023).

[5] K. K. Mishra, A. H. Lone, S. Srinivasan, H. Fariborzi, and G. Setti, Magnetic skyrmion: from fundamental physics to pioneering applications, Appl. Phys. Rev. **12**, 011315 (2025).

[6] N. Romming, C. Hanneken, M. Menzel, J. E. Bickel, B. Wolter, K. von Bergmann, A. Kubetzka, and R. Wiesendanger, Writing and deleting single magnetic skyrmions, Science **341**, 636 (2013).

[7] S. Meyer, M. Perini, S. von Malottki, A. Kubetzka, R. Wiesendanger, K. von Bergmann, and S. Heinze, Isolated zero field sub-10 nm skyrmions in ultrathin Co films, Nature Commun. **10**, 3823 (2019).

[8] C. Moreau-Luchaire, C. Moutafis, N. Reyren, J. Sampaio, N. Van Horne, C. A. F. Vaz, K. Bouzehouane, K. Garcia, C. Deranlot, P. Warnicke, P. Wohlhüter, J. M. George, J. Raabe, V. Cros, and A. Fert, Skyrmions at room temperature: From magnetic thin films to magnetic multilayers, Nature Nanotechnol. **11**, 444 (2016).

[9] W. Legrand, J.-Y. Chauleau, D. Maccariello, N. Reyren, S. Collin, K. Bouzehouane, N. Jaouen, V. Cros, and A. Fert, Hybrid chiral domain walls and skyrmions in magnetic multilayers, Sci. Adv. **4**, eaat0415 (2018).

[10] F. Büttner, I. Lemesh, and G. S. D. Beach, Theory of isolated magnetic skyrmions: From fundamentals to room temperature applications, Sci. Rep. **8**, 4464 (2018).

[11] A. Bernand-Mantel, L. Camosi, A. Wartelle, N. Rougemaille, M. Darques, and L. Ranno, The skyrmion-bubble transition in a ferromagnetic thin film, SciPost. Phys. **4**, 027 (2018).

[12] S. Woo, K. Litzius, B. Kruger, M.-Y. Im, L. Caretta, K. Richter, M. Mann, A. Krone, R. M. Reeve, M. Weigand, P. Agrawal, I. Lemesh, M.-A. Mawass, P. Fischer, M. Kläui, and G. S. D. Beach, Observation of room-temperature magnetic skyrmions and their current-driven dynamics in ultrathin metallic ferromagnets, Nature Mat. **15**, 501 (2016).

[13] W. Legrand, D. Maccariello, N. Reyren, K. Garcia, C. Moutafis, C. Moreau-Luchaire, S. Collin, K. Bouzehouane, V. Cros, and A. Fert, Room-Temperature Current-Induced Generation and Motion of sub-100 nm Skyrmions, Nano Lett. **17**, 2703 (2017).

[14] W. Jiang, X. Zhang, G. Yu, W. Zhang, X. Wang, M. B. Jungfleisch, J. E. Pearson, X. Cheng, O. Heinonen, K. L. Wang, Y. Zhou, A. Hoffmann, and S. G. E. te Velthuis, Direct observation of the skyrmion Hall effect, Nature Physics **13**, 162 (2017).

[15] B. Ivanov, V. Stephanovich, and A. Zhmudskii, Magnetic vortices: The microscopic analogs of magnetic bubbles, J. Magn. Magn. Mater. **88**, 116 (1990).

[16] S. Woo, K. M. Song, X. Zhang, Y. Zhou, M. Ezawa, X. Liu, S. Finizio, J. Raabe, N. J. Lee, S.-I. Kim, S.-Y. Park, Y. Kim, J.-Y. Kim, D. Lee, O. Lee, J. W. Choi, B.-C. Min, H. C. Koo, and J. Chang, Current-driven dynamics and inhibition of the skyrmion Hall effect of ferrimagnetic skyrmions in GdFeCo films, Nature Communications **9**, 959 (2018).

[17] L. Berges, R. Weil, A. Mougin, and J. Sampaio, Reversal of the skyrmion topological deflection across ferrimagnetic angular momentum compensation, Appl. Phys. Lett. **123**, 142404 (2023).

[18] L. Caretta, L. Mann, F. Büttner, K. Ueda, B. Pfau, C. M. Günther, P. Hessing, A. Churikova, C. Klose, M. Schneider, D. Engel, C. Marcus, D. Bono, K. Bagschik, S. Eisebitt, and G. S. D. Beach, Fast current-driven domain walls and small skyrmions in a compensated ferrimagnet, Nature Nanotechnol. **13**, 1154 (2018).

[19] Y. Quessab, J.-W. Xu, E. Cogulu, S. Finizio, J. Raabe, and A. D. Kent, Zero-Field Nucleation and Fast Motion of Skyrmions Induced by Nanosecond Current Pulses in a Ferrimagnetic Thin Film, Nano Lett. **22**, 6091 (2022).

[20] T. Dohi, S. DuttaGupta, S. Fukami, and H. Ohno, Formation and current-induced motion of synthetic antiferromagnetic skyrmion bubbles, Nature Commun. **10**, 5153 (2019).

[21] S. Mallick, Y. Sassi, N. F. Prestes, S. Krishnia, F. Gallego, L. M. Vicente Arche, T. Denneulin, S. Collin, K. Bouzehouane, A. Thiaville, R. E. Dunin-Borkowski, V. Jeudy, A. Fert, N. Reyren, and V. Cros, Driving skyrmions in flow regime in synthetic ferrimagnets, Nature Commun. **15**, 8472 (2024).

[22] V. T. Pham, N. Sisodia, I. D. Manici, J. Urrestarazu-Larrañaga, K. Bairagi, J. Pelloux-Prayer, R. Guedas, L. D. Buda-Prejbeanu, S. Auffret, A. Locatelli, T. O. Menteş, S. Pizzini, P. Kumar, A. Finco, V. Jacques, G. Gaudin, and O. Boulle, Fast current-induced skyrmion motion in synthetic antiferromagnets, Science **384**, 307 (2024).

[23] Y. Jiang, A. Chen, H. Liu, H. Hao, Z. Chen, H. Li, J. Wei, Q. Liu, J. Wang, X. Liu, X. Zhang, and S. Zhang, Current-induced generation and long-distance motion of skyrmions in synthetic antiferromagnetic materials, Appl. Phys. Lett. **127**, 252401 (2025).

[24] M. Bhukta, T. Dohi, K. Leutner, M.-A. Syskaki, F. Kammerbauer, D. M. Tran, S. Wintz, M. Weigand, R. Frömter, and M. Kläui, Antiferromagnetic skyrmion scattering revealed by direct time-resolved imaging of collective dynamics (2025), arXiv 2508.17967.

[25] C. Bran, A. B. Butenko, N. S. Kiselev, U. Wolff, L. Schultz, O. Hellwig, U. K. Rößler, A. N. Bogdanov, and V. Neu, Evolution of stripe and bubble domains in antiferromagnetically coupled $[(\mathrm{Co/Pt})_8/\mathrm{Co/Ru}]_{18}$ multilayers, Phys. Rev. B **79**, 024430 (2009).

[26] C. E. A. Barker, K. Fallon, C. Barton, E. Haltz, T. P. Almeida, S. Villa, C. Kirkbride, F. Maccherozzi, B. Sarpi, S. S. Dhesi, D. McGrouther, S. McVitie, T. A. Moore, O. Kazakova, and C. H. Marrows, Phase coexistence and

transitions between antiferromagnetic and ferromagnetic states in a synthetic antiferromagnet, Phys. Rev. B **109**, 134437 (2024).

[27] M. I. Sim, D. Thian, R. Maddu, X. Chen, H. K. Tan, C. Li, P. Ho, and A. Soumyanarayanan, Zero field antiferromagnetically coupled skyrmions and their field-driven uncoupling in composite chiral multilayers, Adv. Funct. Mater. **35**, 2416927 (2025).

[28] S. Panigrahy, S. Mallick, J. Sampaio, and S. Rohart, Skyrmion inertia in synthetic antiferromagnets, Phys. Rev. B **106**, 144405 (2022).

[29] W. Legrand, D. Maccariello, F. Ajejas, S. Collin, A. Vecchiola, K. Bouzehouane, N. Reyren, V. Cros, and A. Fert, Room-temperature stabilization of antiferromagnetic skyrmions in synthetic antiferromagnets, Nature Mat. **19**, 34 (2020).

[30] A. Finco, P. Kumar, V. T. Pham, J. Urrestarazu-Larrañaga, R. G. Garcia, M. Rollo, O. Boulle, J.-V. Kim, and V. Jacques, Thermal spin wave noise as a probe for the Dzyaloshinskii-Moriya interaction, Phys. Rev. Lett. **135**, 136703 (2025).

[31] X. Chen, T. Tai, H. R. Tan, H. K. Tan, R. Lim, T. S. Suraj, P. Ho, and A. Soumyanarayanan, Tailoring zero-field magnetic skyrmions in chiral multilayers by a duet of interlayer exchange couplings, Adv. Funct. Mater. **34**, 2304560 (2024).

[32] E. Schlömann, Domain walls in bubble films. I. General theory of static properties, J. Appl. Phys. **44**, 1837 (1973).

[33] K. Fallon, S. McVitie, W. Legrand, F. Ajejas, D. Maccariello, S. Collin, V. Cros, and N. Reyren, Quantitative imaging of hybrid chiral spin textures in magnetic multilayer systems by Lorentz microscopy, Phys. Rev. B **100**, 214431 (2019).

[34] J. Lucassen, M. J. Meijer, O. Kurnosikov, H. J. M. Swagten, B. Koopmans, R. Lavrijsen, F. Kloodt-Twesten, R. Frömter, and R. A. Duine, Tuning magnetic chirality by dipolar interactions, Phys. Rev. Lett. **123**, 157201 (2019).

[35] W. Legrand, N. Ronceray, N. Reyren, D. MacCariello, V. Cros, and A. Fert, Modeling the shape of axisymmetric skyrmions in magnetic multilayers, Phys. Rev. Appl. **10**, 064042 (2018).

[36] I. Lemesh and G. S. D. Beach, Twisted domain walls and skyrmions in perpendicularly magnetized multilayers, Phys. Rev. B **98**, 104402 (2018).

[37] C. J. Garcia-Cervera, Structure of the Bloch wall in multilayers, Proc. Roy. Soc. A **461**, 1911 (2005).

[38] A. Bellec, S. Rohart, M. Labrune, J. Miltat, and A. Thiaville, Domain wall structure in magnetic bilayers with perpendicular anisotropy, Europhys. Lett. **91**, 17009 (2010).

[39] N. J. Dubicki, A. Bernand-Mantel, V. V. Slastikov, and C. B. Muratov, Skyrmion stacking in stray field-coupled ultrathin ferromagnetic multilayers, J. Nonlinear Sci. **36**, 7 (2025).

[40] M. C. H. de Jong, D. Khusyainov, J. Hintermayr, B. Sanders, D. Kozodaev, A. V. Kimel, B. Koopmans, T. H. M. Rasing, and R. Lavrijsen, Facilitating electrical and laser-induced skyrmion nucleation with a dipolar-field enhanced effective DMI (2026), arXiv 2602.01818.

[41] A. Hrabec, J. Sampaio, M. Belmeguenai, I. Gross, R. Weil, S. M. Chérif, A. Stashkevich, V. Jacques, A. Thiaville, and S. Rohart, Current-induced skyrmion generation and dynamics in symmetric bilayers, Nature Commun. **8**, 15765 (2017).

[42] L. D. Landau and E. M. Lifshitz, *Course of Theoretical Physics*, Vol. 8 (Pergamon Press, London, 1984).

[43] A. Hubert and R. Schäfer, *Magnetic Domains* (Springer, Berlin, 1998).

[44] A. Bernand-Mantel, A. Fondet, S. Barnova, T. M. Simon, and C. B. Muratov, Theory of magnetic field-stabilized compact skyrmions in thin film ferromagnets, Phys. Rev. B **108**, L161405 (2023).

[45] N. J. Dubicki, *A micromagnetic study of skyrmions in thin-film multilayered ferromagnetic materials* (Ph. D. Thesis, NJIT, 2024).

[46] G. Di Fratta, C. B. Muratov, F. N. Rybakov, and V. V. Slastikov, Variational principles of micromagnetics revisited, SIAM J. Math. Anal. **52**, 3580 (2020).

[47] C. J. García-Cervera, Numerical micromagnetics: A review, Bol. Soc. Esp. Mat. Apl. **39**, 103 (2007).

[48] T. Schrefl, G. Hrkac, S. Bance, D. Süss, O. Ertl, and J. Fidler, Numerical methods in micromagnetics (finite element method), in *Handbook of Magnetism and Advanced Magnetic Materials*, edited by H. Kronmüller and S. Parkin (Wiley-VCH, 2007) pp. 765–794.

[49] E. Kritsikis, A. Vaysset, L. Buda-Prejbeanu, F. Alouges, and J.-C. Toussaint, Beyond first-order finite element schemes in micromagnetics, J. Comp. Phys. **256**, 357 (2014).

[50] S. Fu, W. Cui, M. Hu, R. Chang, M. J. Donahue, and V. Lomakin, Finite-difference micromagnetic solvers with the object-oriented micromagnetic framework on graphics processing units, IEEE Trans. Magn. **52**, 1 (2016).

[51] J. Leliaert, M. Dvornik, J. Mulkers, J. D. Clercq, M. V. Milošević, and B. V. Waeyenberge, Fast micromagnetic simulations on GPU—recent advances made with Mumax3, J. Phys. D: Appl. Phys. **51**, 123002 (2018).

[52] F. N. Rybakov and E. Babaev, Excalibur software (2020), http://quantumandclassical.com/excalibur/.

[53] G. Di Fratta, C. B. Muratov, and V. V. Slastikov, Reduced energies for thin ferromagnetic films with perpendicular anisotropy, Math. Models Methods Appl. Sci. **34**, 1861 (2024).

[54] A. Bernand-Mantel, C. B. Muratov, and T. M. Simon, Unraveling the role of dipolar versus Dzyaloshinskii-Moriya interactions in stabilizing compact magnetic skyrmions, Phys. Rev. B **101**, 045416 (2020).

[55] A. Bernand-Mantel, C. B. Muratov, and T. M. Simon, A quantitative description of skyrmions in ultrathin ferromagnetic films and stability of degree ±1 harmonic maps from $\mathbb{R}^2$ to $\mathbb{S}^2$, Arch. Rat. Mech. Anal. **239**, 219 (2021).

[56] R. M. Corless, G. H. Gonnet, D. E. G. Hare, D. J. Jeffrey, and D. E. Knuth, On the Lambert W function, Adv. Comput. Math. **5**, 329 (1996).

[57] S. Komineas, C. Melcher, and S. Venakides, Chiral skyrmions of large radius, Physica D **418**, 132842 (2021).

[58] S. Rohart and A. Thiaville, Skyrmion confinement in ultrathin film nanostructures in the presence of Dzyaloshinskii-Moriya interaction, Phys. Rev. B **88**, 184422 (2013).

[59] A. Bernand-Mantel, C. B. Muratov, and V. V. Slastikov, A micromagnetic theory of skyrmion lifetime in ultrathin ferromagnetic films, Proc. Natl. Acad. Sci. USA **119**, e2122237119 (2022).

[60] S. Rohart, J. Miltat, and A. Thiaville, Path to collapse for an isolated Néel skyrmion, Phys. Rev. B **93**, 214412 (2016).

[61] B. Heil, A. Rosch, and J. Masell, Universality of annihilation barriers of large magnetic skyrmions in chiral and frustrated magnets, Phys. Rev. B **100**, 134424 (2019).

[62] A. Bernand-Mantel, V. V. Slastikov, and C. B. Muratov, Asymptotically exact formulas for the stripe domains period in ultrathin ferromagnetic films with out-of-plane anisotropy, Phys. Rev. B **111**, 184423 (2025).

[63] M. Belmeguenai, J.-P. Adam, Y. Roussigné, S. Eimer, T. Devolder, J.-V. Kim, S. M. Cherif, A. Stashkevich, and A. Thiaville, Interfacial Dzyaloshinskii-Moriya interaction in perpendicularly magnetized Pt/Co/AlO$_x$ ultrathin films measured by Brillouin light spectroscopy, Phys. Rev. B **91**, 180405 (2015).

[64] C. Eyrich, A. Zamani, W. Huttema, M. Arora, D. Harrison, F. Rashidi, D. Broun, B. Heinrich, O. Mryasov, M. Ahlberg, O. Karis, P. E. Jönsson, M. From, X. Zhu, and E. Girt, Effects of substitution on the exchange stiffness and magnetization of Co films, Phys. Rev. B **90**, 235408 (2014).

[65] Y. Dahmane, S. Auffret, U. Ebels, B. Rodmacq, and B. Dieny, Perpendicular magnetic anisotropy at Co/AlOx interface, IEEE Trans. Magn. **44**, 2865 (2008).

[66] S. Krishnia, L. Vojáček, T. d. C. S. C. Gomes, N. Sebe, F. Ibrahim, J. Li, L. M. Vicente-Arche, S. Collin, T. Denneulin, R. E. Dunin-Borkowski, S. A. Nikolaev, P. Ohresser, N. Jaouen, A. Thiaville, A. Fert, H. Jaffrès, M. Chshiev, N. Reyren, and V. Cros, Interfacial spin-orbitronic effects controlled by different oxidation levels at the Co/Al interface, Phys. Rev. Appl. **24**, 024055 (2025).

[67] J. Nogues, J. Sort, V. Langlais, V. Skumryev, S. Surinach, J. S. Munoz, and M. D. Baro, Exchange bias in nanostructures, Phys. Rep. **422**, 65 (2005).

[68] A. N. Bogdanov and D. A. Yablonskii, Thermodynamically stable "vortices" in magnetically ordered crystals. The mixed state of magnets, Sov. Phys. – JETP **68**, 101 (1989).

[69] A. N. Bogdanov, M. V. Kudinov, and D. A. Yablonskii, Theory of magnetic vortices in easy-axis ferromagnets, Sov. Phys. – Solid State **31**, 1707 (1989).

[70] S. Komineas, C. Melcher, and S. Venakides, The profile of chiral skyrmions of small radius, Nonlinearity **33**, 3395 (2020).

[71] S. Gustafson and L. Wang, Co-rotational chiral magnetic skyrmions near harmonic maps, J. Funct. Anal. **280**, 108867 (2021).

[72] R. Juge, N. Sisodia, J. U. Larrañaga, Q. Zhang, V. T. Pham, K. G. Rana, B. Sarpi, N. Mille, S. Stanescu, R. Belkhou, M.-A. Mawass, N. Novakovic-Marinkovic, F. Kronast, M. Weigand, J. Gräfe, S. Wintz, S. Finizio, J. Raabe, L. Aballe, M. Foerster, M. Belmeguenai, L. D. Buda-Prejbeanu, J. Pelloux-Prayer, J. M. Shaw, H. T. Nembach, L. Ranno, G. Gaudin, and O. Boulle, Skyrmions in synthetic antiferromagnets and their nucleation via electrical current and ultra-fast laser illumination, Nature Commun. **13**, 4807 (2022).

[73] S. Komineas, C. Melcher, and S. Venakides, Chiral magnetic skyrmions across length scales, New J. Phys. **25**, 023013 (2023).

[74] B. Kaplan and G. A. Gehring, The domain structure in ultrathin magnetic films, J. Magn. Magn. Mater. **128**, 111 (1993).

[75] S. V. Tarasenko, A. Stankiewicz, V. . Tarasenko, and J. Ferré, Bloch wall dynamics in ultrathin ferromagnetic films, J. Magn. Magn. Mater. **189**, 19 (1998).

[76] A. Thiaville, S. Rohart, E. Jué, V. Cros, and A. Fert, Dynamics of Dzyaloshinskii domain walls in ultrathin magnetic films, Europhys. Lett. **100**, 57002 (2012).

[77] A. A. Belavin and A. M. Polyakov, Metastable states of two-dimensional isotropic ferromagnets, JETP Lett. **22**, 245 (1975).

[78] L. Desplat, D. Suess, J. V. Kim, and R. L. Stamps, Thermal stability of metastable magnetic skyrmions: Entropic narrowing and significance of internal eigenmodes, Phys. Rev. B **98**, 134407 (2018).

[79] S. von Malottki, P. F. Bessarab, S. Haldar, A. Delin, and S. Heinze, Skyrmion lifetime in ultrathin films, Phys. Rev. B **99**, 060409(R) (2019).

[80] E. H. Lieb and M. Loss, *Analysis* (American Mathematical Society, Providence, RI, 2010).

[81] E. Di Nezza, G. Palatucci, and E. Valdinoci, Hitchhiker's guide to the fractional Sobolev spaces, Bull. Sci. Math. **136**, 521 (2012).

[82] M. Abramowitz and I. Stegun, eds., *Handbook of mathematical functions* (National Bureau of Standards, 1964).

[83] E. Stein, *Harmonic analysis real-variable methods, orthogonality, and oscillatory integrals* (Princeton University Press, Princeton, NJ, 1993).

[84] J. N. Newman and W. L. Frank, An integral containing the square of a bessel function, Math. Comput. **17**, 64 (1963).

[85] I. Gradshteyn and I. Ryzhik, *Table of integrals, series, and products*, 7th ed. (Elsevier/Academic Press, Amsterdam, 2007).